

Do Loop Current Eddies stimulate productivity in the Gulf of Mexico?

Pierre Damien^(1,2), Julio Sheinbaum⁽¹⁾, Orens Pasqueron de Fommervault⁽¹⁾, Julien Jouanno⁽³⁾, Lorena Linacre⁽⁴⁾, Olaf Duteil⁽⁵⁾

⁽¹⁾ Departamento de Oceanografía Física, Centro de Investigación Científica y de Educación Superior de, Ensenada, México,

⁽²⁾ University of California, Los Angeles, CA

⁽³⁾ LEGOS, Université de Toulouse, IRD, CNRS, CNES, UPS, Toulouse, France,

⁽⁴⁾ Departamento de Oceanografía Biológica, Centro de Investigación Científica y de Educación Superior de Ensenada, México,

⁽⁵⁾ GEOMAR Helmholtz Centre for Ocean Research, Kiel, Germany.

Corresponding author: Pierre Damien (pdamien@ucla.edu)

Key Points :

- LCEs trigger a local phytoplankton biomass increase in winter.
- Chlorophyll variability at surface does not reflect the seasonal cycle of the depth-integrated biomass.
- Convective mixing and Ekman pumping are key mechanisms to preferentially supply nutrient toward the euphotic layer in LCEs.

18 **Abstract**

19 Surface chlorophyll concentrations inferred from satellite images suggest a strong influence of
20 the mesoscale activity on biogeochemical variability within the oligotrophic regions of the Gulf of
21 Mexico (GoM). More specifically, long-living anticyclonic Loop Current Eddies (LCEs) are shed
22 episodically from the Loop Current and propagate westward. This study addresses the biogeochemical
23 response of the LCEs to seasonal forcing and show their role in driving phytoplankton biomass
24 distribution in the GoM. Using an eddy resolving ($1/12^\circ$) interannual regional simulation, it is shown
25 that the LCEs foster a large biomass increase in winter in the upper ocean. It is based on the coupled
26 physical-biogeochemical model NEMO-PISCES that yields a realistic representation of the surface
27 chlorophyll distribution. The primary production in the LCEs is larger than the average rate in the
28 surrounding open waters of the GoM. This behavior cannot be directly identified from surface
29 chlorophyll distribution alone since LCEs are associated with a negative surface chlorophyll anomaly
30 all year long. This anomalous biomass increase in the LCEs is explained by the mixed-layer response
31 to winter convective mixing that reaches deeper and nutrient-rich waters.

32 **I/ Introduction**

33 Historical satellite ocean color observations of the deep waters of the Gulf of Mexico (roughly
34 delimited by the 200m isobath and from hereafter referred to as GoM open-waters) indicate low surface
35 chlorophyll concentrations ([CHL]), low biomass and low primary productivity (Müller-Karger et al.,
36 1991; Biggs and Ressler, 2001; Salmerón-García et al., 2011). The GoM open-waters are mostly
37 oligotrophic, as confirmed by more recent bio-optical in-situ measurements from autonomous floats
38 (Green et al., 2014; Pasqueron de Fommervault et al., 2017; Damien et al., 2018). The surface
39 chlorophyll concentration in the GoM open-waters exhibits a clear seasonal cycle which is primarily
40 triggered by the seasonal variation of the mixed layer depth (Müller-Karger et al., 2015) and river
41 discharges (Brokaw et al., 2019). In tandem, the seasonal cycle is strongly modulated by the energetic
42 mesoscale dynamic activity which shapes the distribution of biogeochemical properties (Biggs and
43 Ressler, 2001; Pasqueron de Fommervault et al., 2017). This mesoscale activity is dominated by the
44 large and long-living Loop Currents Eddies (LCEs) which are shed episodically by the Loop Current
45 (Weisberg and Liu, 2017) and constitute the most energetic circulation features in the GoM
46 (Sheinbaum et al., 2016; Sturges & Leben, 2000).

47 Mesoscale activity (see McGillicuddy et al., 2016 for a review) modulates the phytoplankton
48 biomass distribution (Siegel et al., 1999; Doney et al., 2003; Gaube et al., 2014; Mahadevan, 2014) and
49 the ecosystem functioning (McGillicuddy et al., 1998, Oschlies and Garcon, 1998, Garcon et al., 2001).
50 Specifically, the ability of the mesoscale eddies to enhance vertical fluxes of nutrients is determinant in
51 sustaining the observed phytoplankton growth rate in oligotrophic regions such as the GoM open-
52 waters, where the phytoplankton primary production is limited by nutrient availability in the euphotic
53 layer (McGillicuddy and Robinson 1997; McGillicuddy et al., 1998; Oschlies and Garcon, 1998).

54 The upward doming of isopycnals in cyclonic eddies and downward depressions in anticyclonic
55 eddies, also known as “eddy-pumping”, occur when the eddies are strengthening (Siegel et al., 1999,
56 Klein and Lapeyre, 2009) and produce a vertical nutrient transport. This has been historically proposed
57 as the dominant mechanism controlling the mesoscale biogeochemical variability, as it induces a
58 reduction of productivity in the anticyclone and an increase in cyclones. This paradigm is however
59 challenged by observations of enhanced surface chlorophyll concentrations in anticyclonic eddies
60 (Gaube et al., 2014), particularly during winter (Dufois et al., 2016). As a plausible explanation, eddy-
61 wind interactions may significantly modulate vertical fluxes through Ekman transport divergence
62 within the eddies (Martin and Richards, 2001, Gaube et al., 2013, 2015). This mechanism is
63 responsible for a downwelling in the core of cyclones and an upwelling in the core of anticyclones.
64 Dufois et al. (2014, 2016) link these observations to a deeper mixed layer in anticyclonic eddies. This is
65 explained by the eddy-driven modulation of the upper ocean stratification which directly affects the
66 winter convective mixing (He et al., 2017). Observed mixed layers tend to be deeper in anticyclones
67 than in cyclones (Williams, 1998; Kouketsu et al., 2012) and vertical nutrient fluxes to the euphotic
68 layer are potentially enhanced in anticyclones during periods prone to convection (e.g. winter in the
69 GoM). Although some consensus exists on the fundamental role of anticyclonic eddies on the
70 productivity of oligotrophic ocean regions, large uncertainties remain regarding the relative importance
71 of the different mechanisms involved in the biogeochemical responses.

72 Besides, in-situ measurements in oligotrophic regions have shown that the surface [CHL]
73 variability, observed from ocean color satellite imagery, is not necessarily representative of the total
74 phytoplankton (carbon) biomass variability in the water column (Siegel et al., 2013; Mignot et al.,
75 2014). In particular, a surface [CHL] winter increase, may result from physiological mechanisms (i.e.
76 modification of the ratio of [CHL] to phytoplankton carbon biomass) or from a vertical redistribution
77 of the phytoplankton (Mayot et al., 2017) rather than from changes in the biomass content. It is not

78 clear yet which of these hypotheses holds in oligotrophic regions, and more specifically in the GoM
79 open-waters where this issue has been addressed by in-situ sub-surface [CHL] observations (Pasqueron
80 de Fommervault et al., 2017). Most of the studies focusing on chlorophyll variability use surface (or
81 near-surface) [CHL] as a proxy for phytoplankton biomass and interpret a [CHL] increase as an
82 effective biomass production. Only a few studies considered the vertically integrated responses (Dufois
83 et al., 2017; Guo et al., 2017; Huang and Xu, 2018) emphasizing the importance of considering the
84 eddy impact on the subsurface.

85 The objective of this study is to better understand the role of LCEs in driving [CHL] distribution
86 and variability within the GoM open-waters. Material and methods used in this study are presented in
87 section 2. In section 3, the imprint of the LCEs on the surface [CHL] distribution is inferred from
88 satellite ocean color observations. Since these measurements are confined to the oceanic surface layer
89 and do not allow access to the vertical properties of LCEs, we complete the analysis with a coupled
90 physical-biogeochemical simulation (subsections 2 and 3). Particular attention is paid to the validation
91 of the modeled LCE dynamical structures and surface [CHL] anomalies. In the last section, we propose
92 to disentangle the mesoscale mechanisms controlling the seasonal cycle of the [CHL] vertical profile in
93 LCEs. The model also enables to assess both abiotic and biotic processes and physical-biogeochemical
94 interactions that can be difficult to address with in-situ observations only.

95 **II/ Material and methods**

96 **II.1/ The coupled physical-biogeochemical model**

97 The simulation analyzed in this study (referred as GOLFO12-PISCES) has been described and
98 compared with observations in Damien et al. (2018). It relies on a physical-biogeochemical coupled
99 model based on the ocean model NEMO (Nucleus for European Modeling of the Ocean, version 3.6;
100 Madec, 2016) and the biogeochemical model PISCES (Pelagic Interaction Scheme for Carbon and
101 Ecosystem Studies; Aumont and Bopp, 2006; Aumont et al., 2015). The model grid covers the GoM
102 and the western part of the Cayman Sea (Fig 1) with a $1/12^\circ$ horizontal resolution (~ 8.4 km). This
103 allows to resolve scales related to the first baroclinic mode, which is of the order of 30-40 km in the
104 GoM open-waters (e.g., Chelton et al., 1998). The model is forced with realistic open-boundary
105 conditions from the MERCATOR reanalysis GLORYS2V3, high frequency atmospheric forcing based
106 on an ECMWF ERA-interim reanalysis (Brodeau et al., 2010), and freshwater and nutrient-rich
107 discharges from rivers (Dai and Trenberth, 2002). The analysis has been performed using 5-day
108 averaged outputs for a period of 5 years from 2002 to 2007. We refer the reader to Damien et al. (2018)
109 for an extended model and numerical setup descriptions. In this previous study, an extensive validation
110 of the modeled properties were carried out , focusing on physical properties that are known to influence
111 primary production and chlorophyll concentration: the mixed layer depth and the depth and slope of the
112 nutricline. A novel aspect was to use in-situ observations collected from autonomous floats and
113 published in Green et al. (2014) and Fommervault et al. (2017) to validate not only the modeled surface
114 chlorophyll concentration but also the chlorophyll vertical profile in the GoM. To be able to reproduce
115 the vertical profile of chlorophyll correctly, the parameters of the biogeochemical model were largely
116 tuned compared to the ones suitable for global simulations (Aumont et al., 2015). The ability of
117 GOLFO12-PISCES to reproduce the main observed features of the GoM was demonstrated, at least at a
118 basin and seasonal scale.

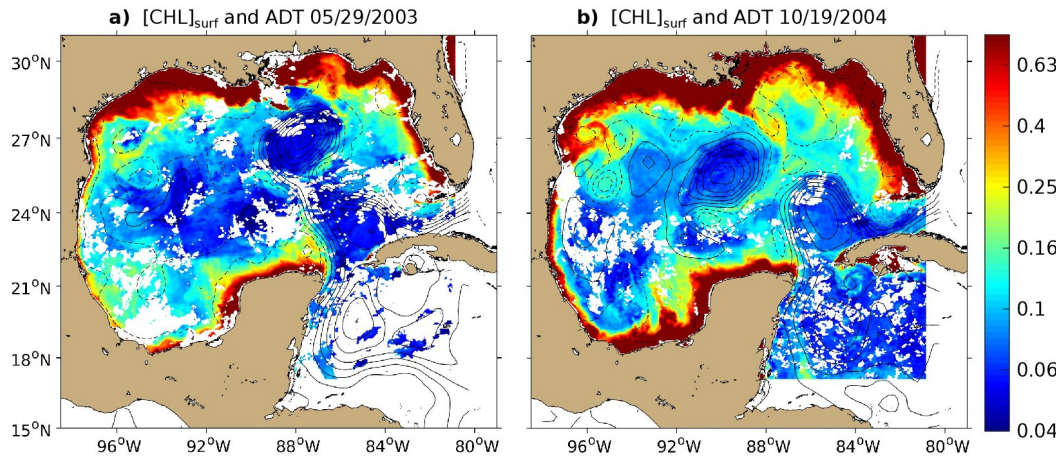


Figure 1: 8-days composite images of $[CHL]_{surf}$ (in $mg \cdot m^{-3}$) around (a) May 29th 2003 and (b) October 19th 2004 derived from Aqua-MODIS images overlaid with contours of Absolute Dynamic Topography (ADT in m) derived from Aviso images are superimposed. Contour interval is 10cm and ADT values lower than 40cm are shown with dashed curves.

II.2/ Observational Data Set Used

Satellite observations are used to evaluate the ability of GOLFO12-PISCES to reproduce the dynamical and biological signatures associated with LCEs. Surface geostrophic velocities are derived from a $1/4^\circ$ multi-satellite merged product of absolute dynamic topography (ADT) provided by AVISO+ (<http://marine.copernicus.eu>). Surface chlorophyll concentrations are from the Aqua-MODIS 4 km product (Sathyendranath et al., 2012; <http://marine.copernicus.eu>) and consist of 8-day composites from 2003 to 2015.

II.3/ LCEs detection, tracking and composite construction

In order to track the LCEs, we use the algorithm developed by Nencioli et al. (2010), which has been extensively employed to track coherent mesoscale eddies (Dong et al., 2012, Ciani et al. 2017, Zhao et al. 2018) and submesoscale eddies (Damien et al., 2017). It is based on the geometric organization of the velocity fields, dominated by rotation, that develop around eddy centers. Here, it is

134 applied to weekly AVISO+ surface geostrophic velocities and GOLFO12-PISCES 5-day averaged
135 velocities at 20m depth. The selection of LCEs is defined using the criteria that eddies have to be shed
136 from the Loop Current.

137 In order to assess the [CHL] response to LCE dynamics, eddy-centric horizontal images and
138 transects of LCEs are used to make composites constructed by averaging modeled variables of the
139 different LCEs collocated to their center. The transect building procedure involves an axisymmetric
140 averaging that assumes axis-symmetry of the dynamical structures and no tilting of their rotation axis.
141 Moreover, we choose not to consider the LCEs formation period and the LCEs destruction period when
142 reaching the western basin (Lipphardt et al., 2008; Hamilton et al., 2018) as LCE destruction/formation
143 involves specific processes (Frolov et al., 2004; Donohue et al., 2016). We therefore focus on the LCEs
144 contained in the central part of the GoM from 86°W to 94°W. Annual composites are computed along
145 with monthly composite averages in order to assess seasonal variability. Composite LCEs averaged
146 during the months of January and February are referred to as winter composites and those averaged
147 during July and August are referred to as summer composites. These composites provide an overview
148 of the LCEs mean hydrographical, biogeochemical and dynamical characteristics.

149 **II.4/ Diagnostics**

150 The LCE radius R_{LCE} is estimated as the radial distance between the center and the peak
151 azimuthal velocity V_{max} . The mixed layer depth (MLD), a major physical factor influencing nutrient
152 distribution and [CHL] dynamics (Mann and Lazier, 2006), is defined as the depth at which potential
153 density exceeds its value at 10m depth by $0.125 \text{ kg} \cdot \text{m}^{-3}$ (Levitus, 1982; Monterey and Levitus, 1997).
154 An important driver of the mixed layer deepening is the stratification of the water column, which is

155 evaluated by the square of the buoyancy frequency $N^2(z) = \frac{-g}{\rho_0} \frac{\partial \rho}{\partial z}$, where g is the gravitational
156 acceleration, z is depth, ρ is density and ρ_0 is a reference density.

157 As carried out in Damien et al. (2018), several metrics are defined and used to describe [CHL]:

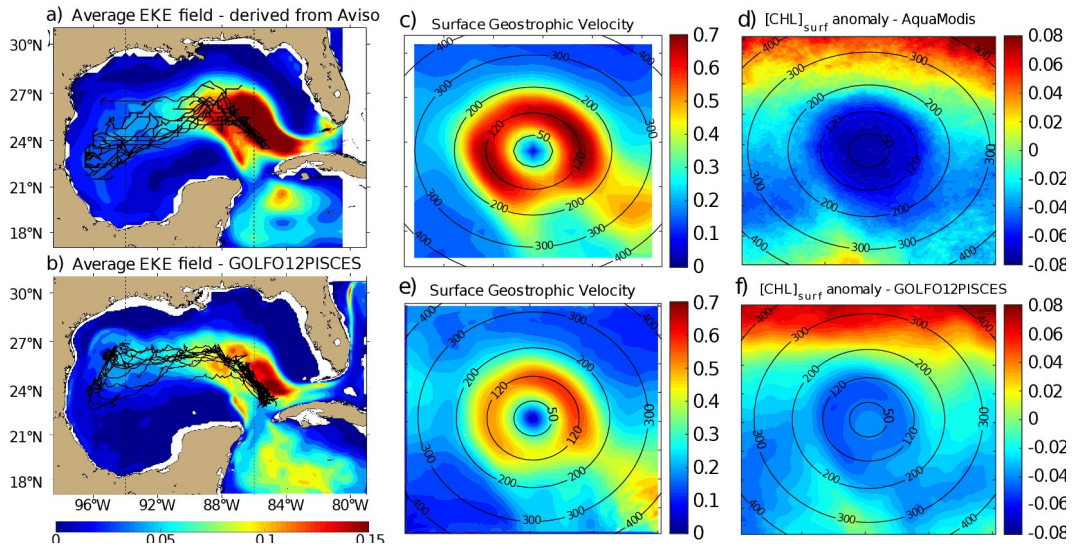
- 158 • [CHL]_{surf}: [CHL] averaged between 0 and 30 m depth, and considered as surface concentration
159 (in mg CHL·m⁻³),
- 160 • [CHL]_{tot}: integrated content of [CHL] over the 0-350 m layer (in mg CHL·m⁻²),
- 161 • DCM: depth of the Deep Chlorophyll maximum (in m),
- 162 • [CHL]_{DCM}: [CHL] value at DCM depth (in mg CHL·m⁻³).

163 To understand the mesoscale distribution of [CHL], key biological variables are vertically integrated
164 between 0 and 350m: the phytoplanktonic concentration [PHY]_{tot}, the primary production rate PP_{tot} and
165 the grazing rate GRZ_{tot}. PP_{tot} consists of two components: new production PPN_{tot} fueled by nutrients
166 supplied from a source external to the mixed layer and regenerated production PPR_{tot} sustained by
167 recycled nutrients within the euphotic layer (Dugdale & Goering, 1967; Eppley & Peterson, 1979),
168 which depth reaches between 120 and 150 m in the GoM (Jolliff et al., 2008; Linacre et al., 2019). A
169 chlorophyll concentration anomaly within LCEs, [CHL]', is computed as $[CHL]' = [CHL] - \overline{[CHL]}$,
170 where $\overline{[CHL]}$ is the averaged background [CHL] field in the open GoM waters (for radius > 250 km from
171 the LCEs' centers). We also define the normalized anomaly as $[CHL]' / SD([CHL]')$ with SD the
172 standard deviation operator, following a similar approach as Gaube et al. (2013, 2014) and Dufois et al.
173 (2016). To limit the influence of very high [CHL] values in coastal waters under the direct influence of
174 continental discharges, a salinity filtering criterion (lower than 36 psu) is applied. A similar method
175 was used by Gaube et al. (2013, 2014) to filter edge effects but using a distance criterion instead.

176 **III/ Results**

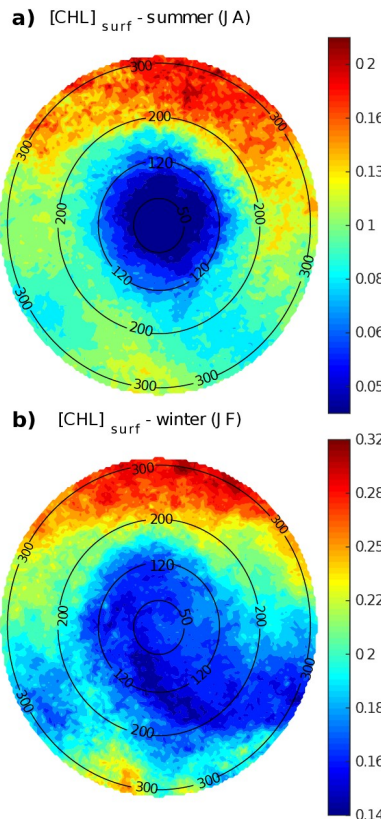
177 **III.1/ Satellite observations of [CHL]**

178 Fig 1 shows the 8-day averaged satellite observations of the surface chlorophyll around May 29th
 179 2003 (a) and October 19th 2004 (b). These observations highlight the strong contrast between the
 180 eutrophic conditions in the coastal waters and the oligotrophic conditions in the open ocean, as already
 181 addressed by several studies (Martinez-Lopez & Zavala-Hidalgo, 2009; Pasqueron de Fommervault et
 182 al., 2017). Far from the coast, these figures also reveal that the surface chlorophyll varies at a scale of
 183 the order of 100km with a distribution that tends to follow the absolute dynamic topography (ADT)
 184 contours.



185 **Figure 2: Average eddy kinetic energy (EKE) field derived from (a) Aviso geostrophic surface velocities and from (b) GOLFO12-**
 186 **PISCES currents at 10m depth. The trajectories of the tracked LCEs are superimposed to the EKE field (black lines). Vertical**
 187 **black dashed lines indicate the central GoM area over which composites are built. Annual LCE composite images of surface**
 188 **geostrophic velocities for (c) Aviso images and (e) GOLFO12-PISCES. Annual LCE composite images of surface chlorophyll**
 189 **concentration anomaly for (d) Modis images and (f) GOLFO12-PISCES. Black circles indicate the radius in kilometers.**

190 LCEs trajectories are reported on Fig 2.a, superimposed onto the geostrophic climatological eddy
 191 kinetic energy (EKE) field at the surface. EKE is computed from eddy velocities defined on each grid
 192 cell as the difference between the total horizontal current and its mean value over 120 days. This time
 193 window is chosen to filter the seasonal signal. EKE is concentrated in the LC and on the westward
 194 pathway of the LCEs (Lipphardt et al. 2008) demonstrating that LCEs constitute the major source of
 195 EKE in the GoM open waters (Sheinbaum et al., 2016; Sturges & Leben, 2000; Hamilton, 2007;
 196 Jouanno et al., 2016).



197 **Figure 3: LCE composite images of $[CHL]_{surf}$ derived from Aqua-MODIS for the (a) summer and (b) winter seasons. Black circles**
 198 **indicate the radius in kilometers.**

199 LCE annual composites of surface geostrophic velocities (Fig 2.c) and $[CHL]_{surf}$ (Fig 2.d) are
 200 built from 482 different satellite images. On average, we found that $R_{LCE} \sim 120$ km and $V_{max} \sim 0.6-0.7$

201 $\text{m}\cdot\text{s}^{-1}$, in agreement with previously reported LCEs (Elliot, 1982; Cooper et al., 1990; Forristal et al.,
202 1992; Glenn and Ebbesmeyer, 1993; Weisberg and Liu, 2017; Tenreiro et al., 2018). LCEs are
203 associated with a negative $[\text{CHL}]_{\text{surf}}$ anomaly ($\sim -0.07 \text{ mg}\cdot\text{m}^{-3}$ in the annual average). The LCEs
204 influence on $[\text{CHL}]_{\text{surf}}$ is largest in summer (Fig 3.a) when it reaches very low values ($< 0.045 \text{ mg}\cdot\text{m}^{-3}$),
205 which corresponds to an anomaly of $\sim -0.08 \text{ mg}\cdot\text{m}^{-3}$. This anomaly is less remarkable in winter (~ -0.06
206 $\text{mg}\cdot\text{m}^{-3}$, Fig 3.b) when $[\text{CHL}]_{\text{surf}} \sim 0.17 \text{ mg}\cdot\text{m}^{-3}$ within LCEs. The high chlorophyll concentrations in the
207 northern part of the composites (in the southern part too but in smaller proportions) are related to
208 shelves.

209 **III.2/ Dynamical characterization of modeled LCEs**

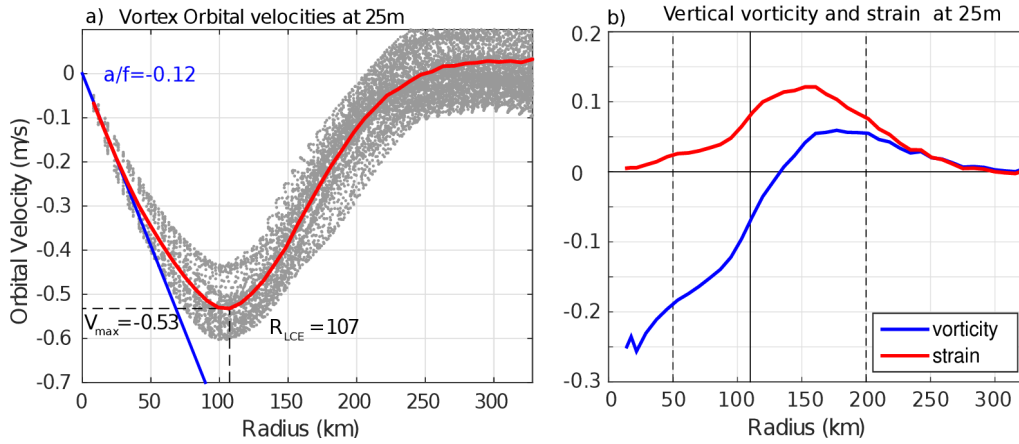
210 A total of 11 model LCEs were detected during the 5 years of simulation. Their trajectories are
211 reported in Fig 2.b, superimposed upon the climatological EKE field simulated at 10 meters. The
212 westward / southwestward propagation of LCEs is well reproduced (Vukovich, 2007) even though the
213 LCEs translation is almost westward in GOLFO12-PISCES. Comparison with Fig 2.a shows the ability
214 of GOLFO12-PISCES to represent the mean and transient dynamical features of the GoM open waters
215 (also see Garcia-Jove et al., 2016).

216 The robustness of the composite method arises from the number of LCE used to build the
217 composites:

- 218 • Annual composite is built from 605 5-day averaged LCEs model outputs from 10 different
219 LCEs,
- 220 • Summer composite is built from 83 5-day averaged LCEs model outputs from 8 different
221 LCEs,

222 • Winter composite is built from 93 5-day averaged LCEs model outputs from 9 different LCEs.

223 The model LCEs surface geostrophic velocities (Fig 2.e) have important similarities with
 224 velocities inferred from altimetry (Fig 2.c) confirming that GOLFO12-PISCES reproduces the surface
 225 signature of the LCEs. However, one can also notice an underestimation of the surface orbital
 226 velocities ($\sim 25\%$ on average over the 50-200 km radius range). This bias could result from the
 227 relatively coarse model resolution and 5-day output frequency that are unable to fully capture the
 228 gradient intensity at R_{LCE} . The assumption of an axial symmetry of the LCE circulation around its
 229 center also induces an error that tends to decrease V_{max} .



230 **Figure 4: (a) Orbital velocities at 25m depth in function of the radius of each detected LCE (light gray dots). The red line is the**
 231 **LCE orbital velocity profile of the annually-averaged composite. (b) Vertical vorticity and strain computed from the averaged**

232 **orbital velocity profile assuming no radial velocity in cylindrical coordinates as $\xi_z = \frac{1}{f r} \frac{\partial r v}{\partial r}$ and $S = \frac{1}{f} (\frac{\partial v}{\partial r} - \frac{v}{r})$.**

233 Orbital velocities of composite eddies are used to distinguish different dynamical areas within
 234 LCEs. The model annual average dynamical profile at 25m depth (Fig 4) reveals a typical vortex-like
 235 structure with $R_{LCE} \sim 107$ km and $V_{max} \sim 0.53 \text{ m}\cdot\text{s}^{-1}$ and suggests the following decomposition:

- $r < 50$ km : the **LCEs core**, where the eddy is approximately in solid body rotation: $V_{\text{orb}} = a \cdot r$ where the coefficient a is related to the Rossby number ($Ro = 2a/f$). The ratio a/f is estimated to be ~ -0.12 (Fig. 4). In this field, the strain is reduced to a minimum and the flow is dominated by rotation.
- $50 \text{ km} < r < 200$ km: the **LCEs ring** structure where the orbital velocity reaches its maximum at R_{LCE} and then decreases. The horizontal strain is important in this field, even dominating vorticity from radius exceeding R_{LCE} .
- $r > 200$ km: the **background GoM**, where the velocity anomalies related to the LCE vanish.

In the vertical (Fig 5.a), LCEs are near-surface intensified anticyclonic vortex rings. At depth, the orbital peak velocity decreases rapidly. At 500 m depth, $V_{\text{max}} \sim 0.17 \text{ m} \cdot \text{s}^{-1}$ and $R_{\text{LCE}} \sim 75$ km, and the dynamical LCE signal nearly vanishes below 1500 m depth ($V_{\text{max}} < 0.03 \text{ m} \cdot \text{s}^{-1}$). The proposed division into 3 distinct dynamical regions applies from the surface down to 500 m depth (Fig 5.a).

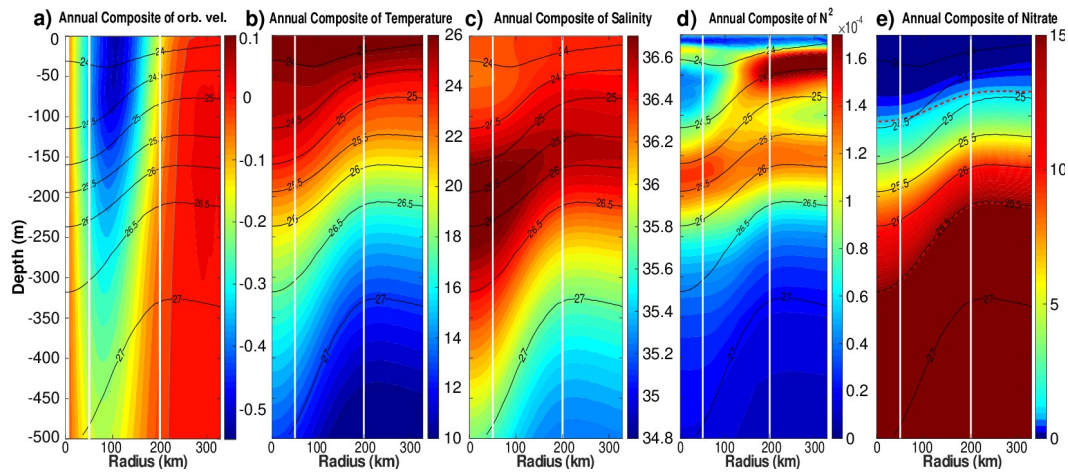


Figure 5: Annually-averaged LCE composite transects of (a) orbital velocities [m/s], (b) potential temperature [°C], (c) salinity [psu], (d) squared Brunt-Väisälä frequency (N^2 in s^{-2}) and (e) nitrate concentration [$\text{mmol} \cdot \text{m}^{-3}$]. Isopycnals anomalies (black contours) are superimposed on all panels. Vertical white lines delimit the three dynamical fields of the LCE composite. On panel e, dashed red lines highlights two specific iso-nitrate contours: 1 and 15 $\text{mmol} \cdot \text{m}^{-3}$.

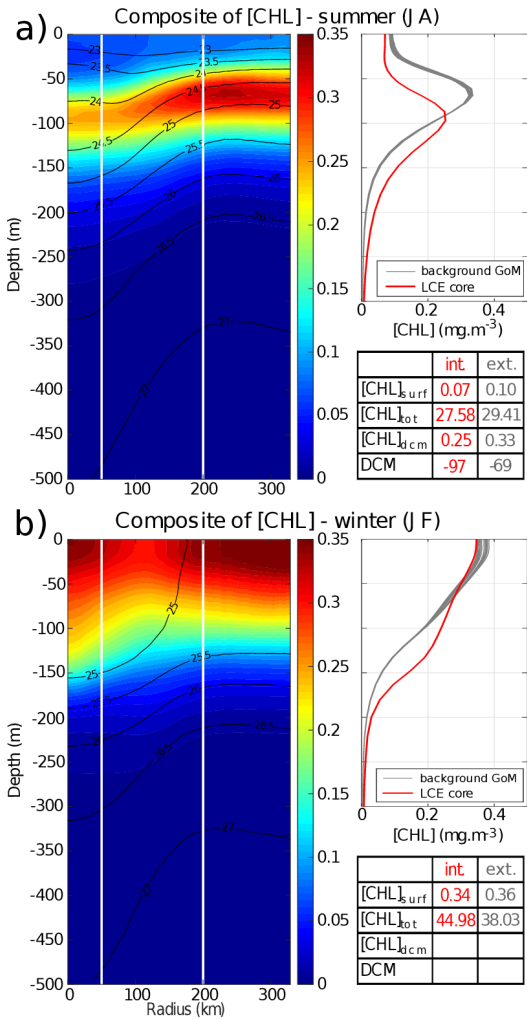
252 The composite hydrological structure of modeled LCEs is shown in Fig 5.b and 5.c. The
253 depression of isopycnals, associated with a depression of isotherms and isohalines, is characteristic of
254 oceanic anticyclones. In the core of the eddies, the composite depicts a salinity maximum located
255 between 100 and 300 m, corresponding to the signature of the Atlantic Subtropical UnderWater
256 (ASTUW) of Caribbean origin entering the GoM through the Yucatan Channel (Badan et al., 2005;
257 Hernandez-Guerra & Joyce, 2000; Wuust, 1964). This salinity maximum is not limited to the core of
258 the LCE but gradually erodes and shallows: 36.82 psu at 200 m in the LCEs core and 36.61 psu at 150
259 m in the background GoM common water. Details on the fate of this salinity maximum investigated
260 with GOLFO12 simulations can be found in Sosa-Gutiérrez et al. (2020). The ASTUW layer (salinity >
261 36.5 psu) is also thicker in the LCEs core (~190 m thick) compared to the background GoM water
262 (~120 m thick). Overall, GOLFO12-PISCES reproduces the observed hydrological structure of LCEs
263 (Elliott, 1982; LeHenaff et al., 2012; Hamilton et al., 2018; Meunier et al., 2018b).

264 The annually averaged LCE composite presents a lens-shaped structure exhibiting a ~50 m thick
265 layer of weakly stratified waters located between 50 and 100 m depth (Fig 5.d). This subsurface modal
266 water presents hydrological characteristics close to the observed background GoM waters (potential
267 temperature ~25.4°C and salinity ~ 36.3 psu, Meunier et al., 2018b) and is surrounded below and above
268 by well stratified layers (Meunier et al., 2018a). The upper pycnocline varies seasonally and vanishes in
269 winter due to the deepening of the mixed layer, whereas the lower pycnocline is permanent.

270 The downward displacement of isopycnals is associated with a depletion of nutrients in the upper
271 layer of the LCEs core (Fig 5.e). This is a typical feature of mesoscale anticyclones in the ocean
272 (McGillicuddy et al. 1998; Oschlies and Garcon, 1998). The 1 mmol.m⁻³ iso-nitrate concentration
273 (hereafter Z_{NO_3} , sometimes referred to as the nitracline as in Cullen & Eppley, 1981; Pasqueron de
274 Fommervault et al., 2017 or Damien et al., 2018) is located at ~ 70 m depth in the background GoM

275 waters whereas it is found much deeper in the core ($Z_{NO_3} \sim 106$ m). At depth, iso-nitrate layers and
 276 isopycnals are well correlated (Ascani et al., 2013; Omand & Mahadevan, 2014). For instance, iso-
 277 nitrate concentration of $15 \text{ mmol}\cdot\text{m}^{-3}$ follows the displacements of the $1026.5 \text{ kg}\cdot\text{m}^{-3}$ isopycnal.
 278 However, above 150 m, the density/nitrate relation is different inside and outside the eddies (Z_{NO_3} is
 279 collocated with isopycnal $1024.4 \text{ kg}\cdot\text{m}^{-3}$ in the LCEs core while it is on isopycnal $1024.9 \text{ kg}\cdot\text{m}^{-3}$ in the
 280 background GoM).

281 **III.3/ Surface and vertical distribution of chlorophyll in LCEs**



282 **Figure 6: LCE composite transects of [CHL] during summer season (A) and winter season (B). Density anomalies (black**
 283 **contours) are superimposed. Vertical white lines delimit the three dynamical fields of the LCE composite. For each season, [CHL]**

profiles in the LCE core ($r < 50$ km, red lines) and in the background GoM ($200 \text{ km} < r < 330$ km, gray lines) are plotted. Key metrics concerning [CHL] profiles are also indicated in the tables.

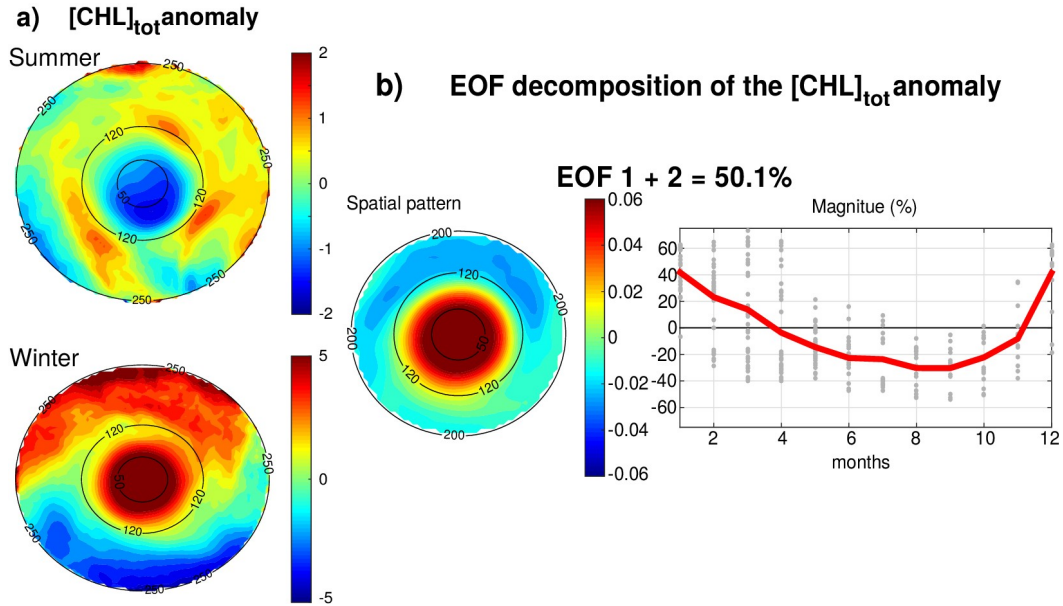
The large difference in stratification between the LCEs core and background GoM suggests a contrasted seasonal response of the [CHL]. This is evidenced by $[\text{CHL}]_{\text{surf}}$ observation (Fig 2.d), with a good model agreement (Fig. 2.f), and is confirmed by the analysis of summer and winter composites of [CHL] vertical distribution:

- In summer (Fig 6.a), $[\text{CHL}]_{\text{surf}}$ is $\sim 30\%$ lower in the LCEs core ($r < 50\text{km}$) than in the background GoM ($200 \text{ km} < r < 330 \text{ km}$). A pronounced DCM, characteristic of oligotrophic environments, is deeper in the core ($\sim 97 \text{ m}$) than in the background GoM ($\sim 69 \text{ m}$) with chlorophyll concentrations significantly lower in the interior ($\sim -25\%$).
- In winter, the [CHL] is maximum at the surface in all the composite domains (Fig 6.b). $[\text{CHL}]_{\text{surf}}$ is lower in the LCEs core compared to the background GoM but the difference is less marked ($\sim -6\%$) than in summer. The main discrepancy is the depth of the inflection point of these profiles. It is deeper in the LCEs core ($\sim 150 \text{ m}$), resulting in a more homogenized [CHL] over a deeper layer than in the background GoM ($\sim 120 \text{ m}$).

However, despite reduced surface concentration both in winter and summer, the integrated chlorophyll content, $[\text{CHL}]_{\text{tot}}$, shows a distinct seasonal pattern compared to the surface (tables in Fig 6):

- In summer, $[\text{CHL}]_{\text{tot}}$ is lower in the LCEs core ($27.58 \text{ mg}\cdot\text{m}^{-2}$) compared to the background GoM ($29.41 \text{ mg}\cdot\text{m}^{-2}$) and $\Delta[\text{CHL}]_{\text{tot}} = -1.83 \text{ mg}\cdot\text{m}^{-2}$,
- In winter, $[\text{CHL}]_{\text{tot}}$ is higher in the LCEs core ($44.98 \text{ mg}\cdot\text{m}^{-2}$) compared to the background GoM ($38.03 \text{ mg}\cdot\text{m}^{-2}$) and $\Delta[\text{CHL}]_{\text{tot}} = +6.95 \text{ mg}\cdot\text{m}^{-2}$.

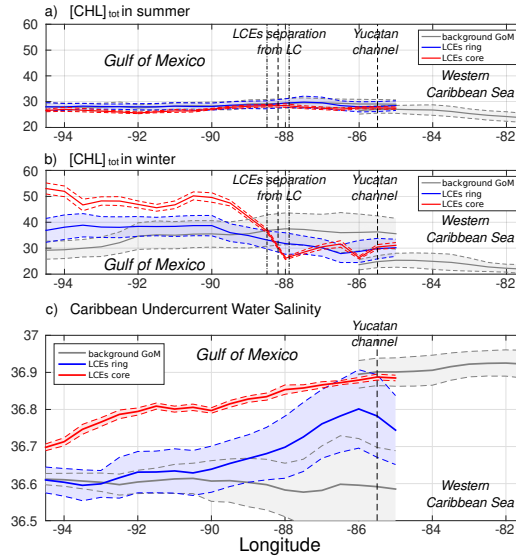
306 The winter increase of $[\text{CHL}]_{\text{tot}}$ is around 29% in the background GoM whereas it reaches 63% in the
 307 LCEs core, leading to $[\text{CHL}]_{\text{tot}}$ in the core being larger than $[\text{CHL}]_{\text{tot}}$ in the background GoM in winter.
 308 Meanwhile, $[\text{CHL}]_{\text{surf}}$ remains lower within the LCEs core. The fact that the $[\text{CHL}]$ at the surface does
 309 not reflect its depth-integrated behavior means that the peculiar variability of $[\text{CHL}]$ within LCEs may
 310 not be fully captured by ocean color satellite measurements. This is consistent with Pasqueron de
 311 Fommervault et al. (2017) and Damien et al. (2018) observations and modeling results which addressed
 312 the vertical $[\text{CHL}]$ distribution in the GoM.



313 **Figure 7: (a) Anomaly of $[\text{CHL}]_{\text{tot}}$ in summer and winter seasons. Black circles indicate the radius in kilometers. (b) EOF**
 314 **decomposition of the normalized $[\text{CHL}]_{\text{tot}}$ anomaly. The spatial patterns and monthly magnitude (gray dots; the red line**
 315 **represents their monthly averaged value) of the two first modes are indicated. Modes 1 and 2 were summed together (upper**
 316 **panel) and represent 50.1% of the total variance.**

317 $[\text{CHL}]_{\text{tot}}$ is strongly shaped by both the seasonal variability and the LCEs. The seasonal
 318 composites of $[\text{CHL}]_{\text{tot}}$, shown in Fig 7.a, confirm the summer/winter contrast and highlight a
 319 monopole structure with a relatively homogeneous distribution of $[\text{CHL}]_{\text{tot}}$ within the eddy's core. In
 320 order to better characterize the spatio-temporal variability of $[\text{CHL}]_{\text{tot}}$ induced by LCEs, an Empirical

321 Orthogonal Function (EOF) analysis was performed on the normalized $[\text{CHL}]_{\text{tot}}$ anomaly (Fig 7.b)
 322 following the methodology of Dufois et al. (2016). It consists in decomposing the signal into
 323 orthogonal modes of variability. Here, we choose to focus on the first two most significant modes
 324 which explain 40.2% and 9.9% of the variability. Since they both depict a similar monopole structure
 325 in the LCEs core, they were added up in a mode referred to EOF 1+2 responsible for 50% of the total
 326 $[\text{CHL}]_{\text{tot}}$ variance within LCEs. The third eigenmode (not shown) accounts for 6.2% and depicts a
 327 dipole structure with opposite polarity located at the east and north of the eddy center. On average, the
 328 EOF1+2 mode is positive in winter (from December to March) and negative the rest of the year (from
 329 April to November), with a maximum in January December and a minimum in September. This
 330 justifies, a posteriori, the choice to consider winter and summer LCE composites.



331 **Figure 8: (a) Summer $[\text{CHL}]_{\text{tot}}$, (b) winter $[\text{CHL}]_{\text{tot}}$ and (c) salinity of Caribbean waters (ASTUW defined as the subsurface**
 332 **salinity maximum) as a function of longitude in (red) the LCEs core, (blue) the LCEs ring and in (gray) the background GoM.**
 333 **Full lines indicate the averaged value and dashed lines the +/- one standard deviation interval.**

334 The composite evolution of the LCEs $[\text{CHL}]_{\text{tot}}$ along their westward journey is shown in Fig 8.a
335 and 8.b. It illustrates how the total chlorophyll concentration is preferentially increased in winter within
336 the LCEs core, as soon as the LCEs are shed from the LC. The winter $[\text{CHL}]_{\text{tot}}$ within LCEs is much
337 larger (exceeding one standard deviation) than the background winter $[\text{CHL}]_{\text{tot}}$. In terms of integrated
338 $[\text{CHL}]$, the LCEs-induced seasonal variability overwhelms the GoM open-waters background seasonal
339 variability.

340 **IV/ Discussion**

341 In an oligotrophic environment such as the GoM open-waters, the primary production is
342 generally limited by nutrient supply and $[\text{CHL}]_{\text{tot}}$ exhibits low seasonal variability at the GoM basin
343 scale (Pasqueron de Fommervault et al., 2017). The winter increase of $[\text{CHL}]_{\text{tot}}$ within the LCEs core
344 (which translates into an effective increase of biomass, see appendix A) contrasts and may have large
345 implications for the regional biogeochemical cycles and ecosystem structuration. It also echoes several
346 studies which report elevated $[\text{CHL}]_{\text{surf}}$ within anticyclonic eddies in the oligotrophic subtropical gyre
347 of the southeastern Indian Ocean (Martin and Richards, 2001; Waite et al., 2007; Gaube et al., 2013;
348 Dufois et al., 2016, 2017; He et al., 2017), questioning the classical paradigm of low productivity
349 usually associated with anticyclonic eddies.

350 The mechanisms explaining the LCE impact on $[\text{CHL}]$ are discussed below, trying to rationalize
351 the respective role of abiotic (e.g., trapping, winter mixing, Ekman pumping) and biotic processes (e.g.,
352 primary production (PP), grazing pressure, regenerated versus new PP).

IV.1 Eddy trapping

The distinct hydrological and biogeochemical properties associated with the LCEs core suggest their ability to trap and transport oceanic properties. This mechanism, known as the eddy-trapping (Early et al., 2011; Lehahn et al., 2011; McGillicuddy, 2015; Gaube et al., 2017), is efficient only if the orbital velocities of the vortex are faster than the eddy propagation speed (Flierl, 1981; d'Ovidio et al., 2013). The rotational velocities of the model LCEs are $\sim 0.53 \text{ m} \cdot \text{s}^{-1}$ are one order of magnitude larger than the propagation velocities ($\sim 0.046 \text{ m} \cdot \text{s}^{-1}$ on average). This suggests that LCEs might have a certain ability to trap the water masses present in their core with relatively low exchanges with the exterior.

Salinity is well-suited to investigate water masses trapped within the LCEs core during their propagation toward the western GoM (Fig 8.c; Sosa-Gutierrez et al., 2020): salinity distribution shows a marked subsurface maximum that is not affected by biogeochemical processes. In the Western Caribbean Sea, ASTUW is characterized by high salinity (~ 36.9 psu on average) and low standard deviation (< 0.05 psu). The eastern GoM salinity field reveals that most of the ASTUW crosses the Yucatan Channel within the Loop Current. During the formation of LCEs, a significant part of ASTUW is captured into the LCEs core with low alteration of its properties (Fig 5.c and 8.c). Within the LCEs core, the water mass is transported from eastern to the western GoM where its salinity decreases from 36.9 psu to 36.7 psu. Although altered, the ASTUW signature is still clearly detectable in the GoM western boundary. The other part of ASTUW entering the GoM is found in the LCEs ring. Compared to the core, the salinity in the ring is on average lower (~ 36.8 psu in the eastern GoM) and presents a high standard deviation, pointing out that more recent ASTUW co-exists with older ASTUW that yields lower salinity maxima. As LCEs travel westward across the GoM, salinity in the LCEs ring

375 decays rapidly to reach values similar to the background GoM values (~ 36.6 psu). This
376 homogenization mainly arises from vertical mixing and winter mixed layer convection (Sosa-Gutierrez
377 et al., 2020). Horizontal intrusions and filamentation may also contribute to this homogenization
378 (Meunier et al., 2020). The composites also suggest that almost no ASTUW enters the GoM apart from
379 the LCEs. The slight increase of the background salinity from eastern to western GoM is a consequence
380 of the diffusion of salt from the LCEs toward the exterior.

381 Although LCEs undergo considerable decaying rates, their erosion is particularly strong in the
382 ring while the core remains better isolated from the surrounding waters (Lehahn et al., 2011; Bracco et
383 al., 2017). Since no significant $[\text{CHL}]_{\text{tot}}$ seasonal variability is reported in the Western Caribbean Sea
384 (Fig. 8), the biogeochemical behavior in the LCEs core has then to be driven by local processes with
385 low influence of horizontal advective process from the ring or of the Caribbean waters trapped during
386 the LCEs formation. Given that the LCEs core is also quite homogeneous, the following discussion
387 relies on the analysis of the seasonal cycles of selected parameters averaged within the LCEs core.

388 **IV.2 Nitracline depth and nutrient supply into the mixed layer**

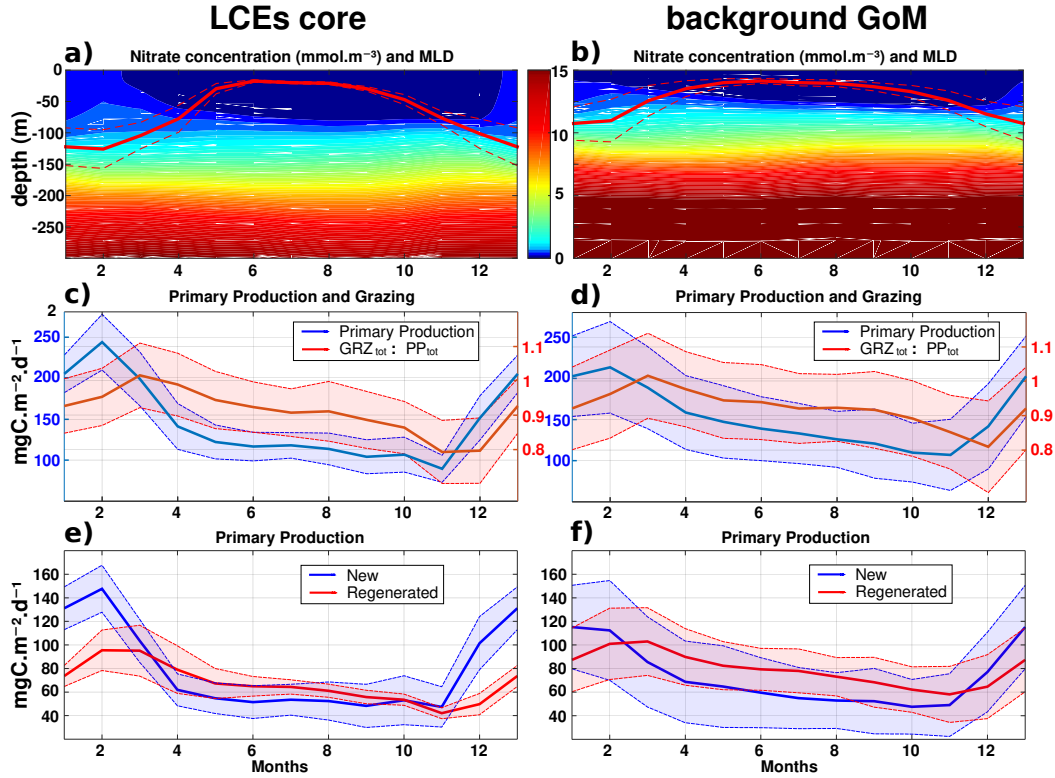


Figure 9: Climatological seasonal cycles of (a and b) nitrate concentration profiles (the red line overlaid is the average mixed layer depth), (c and d) the total primary production (blue) and the ratio of grazing rate over primary production (red) and (e and f) the new (blue) and regenerated (red) primary production. The left panels (a, c and e) refer to the seasonal time series in the LCEs core ($r < 50$ km) whereas the right panels (b, d and f) refer to the seasonal time series in the background GoM ($r > 200$ km). For each average cycle, the mean value is shown (full line) along with its variability (± 1 standard deviation relative to the mean, dashed lines).

The LCEs impact the upper ocean stratification (Fig 5.d), the nutricline depth (Fig 5.e) and consequently the nutrient supply to the euphotic layer (McGillicuddy et al., 2015). The relationship between mixed layer deepening and nutrient supply is studied here by comparing the Z_{NO_3} with the MLD (Fig 9.a,b).

399 In late-spring and summer (from May to September), the water column is stratified (shallow
 400 MLD) and the downward displacement of the isopycnals within the LCEs pushes nutrients below the
 401 euphotic zone (see also Figs 5.e, 6.a): less nutrients are available within the LCE cores for
 402 phytoplankton growth, explaining a deeper and less intense DCM. In winter, the convective mixing,
 403 fostered both by intense buoyancy losses and strong mechanical energy input at the surface, causes a
 404 larger deepening of the mixed layer within the LCEs core (~ -125 m, Fig 9.a) compared to the
 405 background (~ -85 m, Fig 9.b). This asymmetry is due to a pronounced decrease of the surface and
 406 subsurface stratification within the LCE core (Fig 5.d, Kouketsu et al., 2012). A quantitative diagnostic
 407 of the stratification is given by the columnar buoyancy, $\int_0^H N^2(z) \cdot z \cdot dz$ which measures the buoyancy
 408 loss required to mix the water column to a depth H (Herrmann et al. 2008). Fig 10.a reveals significant
 409 differences in pre-winter buoyancy between the eddy core and its surroundings. Assuming that the
 410 change in buoyancy content is mainly controlled by the buoyancy flux at the surface (see Turner 1973;
 411 Lascaratos & Nittis, 1998), it suggests that mixing the water column down to ~ -210 m depth requires
 412 smaller surface buoyancy loss in LCEs cores compared to the background GoM (Fig 10.b).

413 However, the larger winter deepening of the mixed layer within the LCEs core is not a sufficient
 414 condition to explain a larger nutrient supply. Indeed, it fosters the transport of nutrients from the
 415 nitracline toward the mixed layer because both are getting closer. Fig 10.c highlights that a smaller
 416 buoyancy loss mixes down the water column to greater nutrient concentration levels in the LCEs core
 417 compared to the LCEs surrounding. This likely explains the winter increase of surface nitrate
 418 concentration within the LCEs (Fig 9.a). In addition, a diagnostic of the different contributions to
 419 $[\text{NO}_3]$ evolution is proposed in appendix B. It shows the dominant role of vertical advection and
 420 diffusion in winter in providing nutrients to the euphotic layer in the LCEs core.

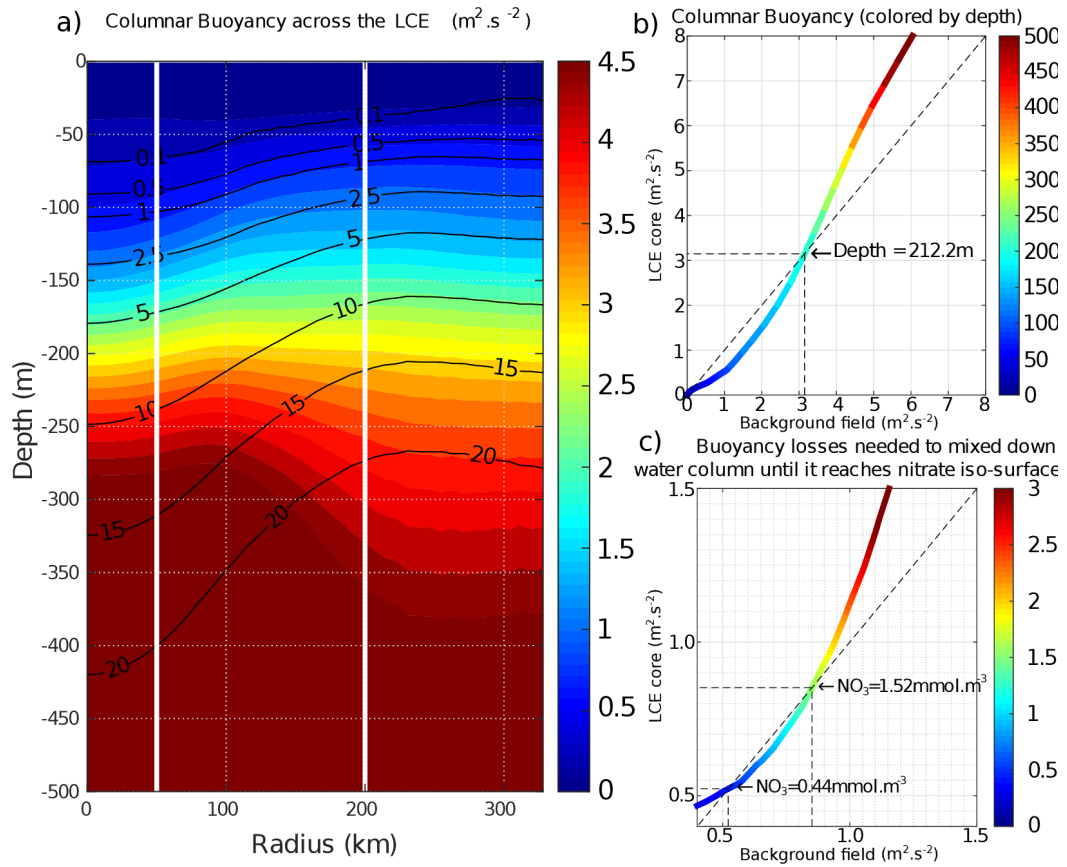


Figure 10: (a) Columnar Buoyancy transect composite in summer, corresponding to pre-winter mixing season. Iso-nitrate concentrations (black contours) are superimposed. Vertical white lines delimit the three dynamical fields of the LCE composite. (b) Vertical increase of the columnar buoyancy in the LCEs core versus the background GoM. Colors refer to depth. (c) Columnar buoyancy loss required to mix the water column down to the iso-nitrate surface defined by the line color.

So far we have assumed that the surface buoyancy fluxes are identical over the LCEs core and the background GoM. However, this is not strictly the case because temperature/salinity features in the LCEs and background waters are different (Fig 5.b,c; see also Williams 1988). The modeled surface buoyancy loss during winter season is $\sim 18\%$ more intense within the LCEs. This difference is substantial and probably mainly driven by additional surface cooling applied on the warm LCE core through air-sea interaction. It contributes to enhance convection within the eddies core, and then nutrient supply toward the surface.

IV.3 Productivity and grazing

The primary productivity PP_{tot} presents a clear seasonal cycle both in the LCEs cores and in the background GoM with lower values in October-November, a sharp increase starting in November, a maximum in February and a gradual decrease from March to October (Fig 9.c.d). The annual PP_{tot} is slightly lower in the LCEs core ($\sim 142.4 \text{ mgC} \cdot \text{m}^{-2} \cdot \text{d}^{-1}$) than in the background GoM ($\sim 148.9 \text{ mgC} \cdot \text{m}^{-2} \cdot \text{d}^{-1}$). The amplitude of the seasonal cycle is larger in the LCEs core: from April to November, PP_{tot} is on average $\sim 12\%$ lower in the LCEs core whereas, in winter, PP_{tot} is $\sim 14\%$ higher where it reaches $\sim 243.2 \text{ mgC} \cdot \text{m}^{-2} \cdot \text{d}^{-1}$ in February. Particularly in the LCE core, the PP_{tot} seasonal cycle is tightly correlated with vertical mixing revealing the important role of mixing in the biogeochemistry. The relatively low standard deviation of the monthly PP_{tot} distribution in the LCE core also supports the idea that the influence of the seasonal variability of the forcing largely overwhelms their interannual and sub-monthly variability.

The ratio of the PPN_{tot} and PPR_{tot} provides information about the mechanisms controlling the biomass growth (Fig 9.e and 9.f). In winter, the PPN_{tot} plays a leading role, reaching up to $113\text{-}147 \text{ mgC} \cdot \text{m}^{-2} \cdot \text{d}^{-1}$, driven by the winter mixing and induced NO_3 fluxes (see Appendix B). Conversely, the PPR_{tot} is dominant from April to October. During this period, low NO_3 resources are available in the euphotic layer and the ecosystem preferentially uses ammonium to sustain the PP_{tot} . This seasonal pattern is characteristic of oligotrophic environments such as the GoM open waters (Wawrik et al., 2004; Linacre et al., 2015). In winter, changes in PP_{tot} are correlated to the intensity of winter mixing in the LCEs core (Fig 9.c) and the background GoM (Fig 9.d). The larger PPN_{tot} in the eddy core is

452 consistent with a larger supply of NO_3 and evidences that the core of anticyclones can be preferential
453 spots of enhanced biological production.

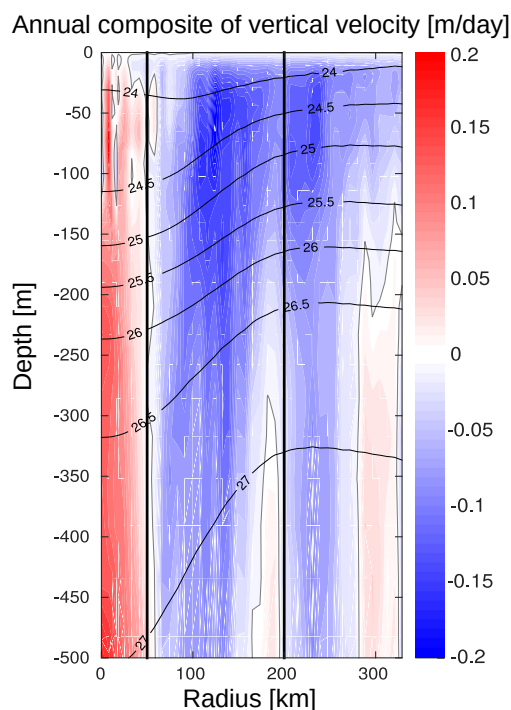
454 The pressure exerted by zooplankton grazers varies seasonally (Fig 9.c.d). It shows a similar
455 seasonal cycle in the LCEs core and in the background GoM. On average, $\sim 90\%$ of the total growth is
456 consumed by grazers, reaching the highest impact in March, just one month after the peak season of the
457 PP_{tot} in both areas. In February the difference between the primary production and the grazing rate is
458 larger in the LCEs core than in the GoM background (Fig. 9.c), leading to an enhanced net primary
459 production. Considering the ecosystem from a “top-down” perspective, the grazing rate also
460 participates then in enhancing $[\text{CHL}]_{\text{tot}}$ within the LCEs core compared to the background.

461 **IV.4 How to explain summer productivity?**

462 In summer, the total primary production is higher in the background GoM waters as the
463 regenerated production rate is higher. Since grazing is known to be a major source of recycled nutrients
464 in the euphotic zone (Sherr and Sherr, 2002), the lower grazing rate inside the LCE during summer
465 (Fig. 9.c.d.) likely explains this lower regenerated production. In addition, production of organic matter
466 occurs in a deeper layer within the LCEs core compared to the background GoM (Fig. B1. e. f.). It is
467 then more likely exported out of the euphotic layer in the form of settling particle, leading to lower
468 remineralization rates in the upper layers to feed regenerated production. More surprising, the new
469 primary production exhibits similar rates in both regions, although NO_3 depletion occurs deeper in the
470 LCEs core. In the absence of a strong enough vertical mixing when the mixed layer is shallow, this
471 apparent mismatch requires an additional mechanism, vertical advection, capable to supply NO_3 to the
472 euphotic layer (Sweeney et al., 2003; McGillicuddy et al., 2015).

473 The model vertical velocity in the LCEs reveals an upward pumping in their core (Fig 11). The
 474 vertical velocity between 100 and 500 m is on average $+0.07 \text{ m} \cdot \text{day}^{-1}$. This vertical transport is mainly
 475 driven by two mechanisms, eddy pumping (Falkowski et al., 1991) and eddy-wind interaction (Dewar
 476 and Flierl, 1987), but their relative importance is difficult to quantify (Gaube et al. 2014; McGillicuddy
 477 et al., 2015).

478 The eddy pumping mechanism is related to the decay of the rotational velocities from the
 479 moment LCEs are released from the Loop Current. In the LCE core, this decay is considered as
 480 moderate since lateral diffusivity is expected to be relatively low (section V.1). This process may
 481 however be considerable in the LCE ring where the erosion rates are important (Meunier et al., 2020).



482 **Figure 11: Annually-averaged LCE composite transects of vertical velocities (m/day). Isopycnals anomalies (black contours) are**
 483 **superimposed on all panels. Vertical white lines delimit the three dynamical fields of the LCE composite.**

484 Eddy-wind interactions are due to mesoscale modulation of the Ekman transport. Following the
 485 observation of a LCE core in quasi-solid body rotation, the horizontal vorticity varies little with the
 486 radius resulting in a negligible “non-linear” contribution of the Ekman pumping (McGillicuddy et al.,
 487 2008; Gaube et al., 2015). Assuming a small effect of the eddy SST-induced Ekman pumping, the total
 488 Ekman pumping simplifies into its “linear” contribution computed as $W_E = \frac{\nabla \times \tau}{\rho_0 \cdot (f + \xi)}$, where ρ_0 is the
 489 surface density, f the Coriolis parameter, τ the stress at the sea surface depending on both the wind and
 490 ocean currents at the surface (Martin and Richards, 2001, equation 12) and $\nabla \times$ the curl operator.
 491 Considering uniform wind velocities ranging from 4.5 to 7.5 m·s⁻¹ (Nowlin & Parker, 1974;
 492 Passalacqua et al., 2016) blowing over the LCE, the curl of the stress arises from the anticyclonic
 493 surface circulation generated by the eddy. Its manifestation is a persistent horizontal divergence at
 494 surface balanced by an upward pumping in the eddy interior (see Martin & Richards, 2001; Gaube et
 495 al., 2013, 2014 for further details). With $\rho_0 \sim 1023 \text{ kg} \cdot \text{m}^{-3}$ and $f \sim 6.2 \cdot 10^{-5} \text{ s}^{-1}$, we estimate W_E to range
 496 from + 0.06 to 0.13 m·day⁻¹, in agreement with the modeled vertical velocity within the core. The
 497 Ekman-eddy pumping mechanism could explain a large fraction of the gradual upwelling within the
 498 eddy’s core (Fig. 11) and may actively contribute to the advective vertical flux of nutrients (see
 499 Appendix B). In summer, this mechanism could explain why new primary production rates are similar
 500 in the LCEs core and the background GoM waters although the nutrient pool is located much deeper in
 501 the LCEs core.

502 The eddy-Ekman pumping persists in the LCEs core throughout their lifetime as long as there is
 503 a wind stress applied at the surface. During wintertime, we expect that both vertical mixing and eddy-
 504 Ekman pumping participate to increase the new primary production. A question then arises on the

relative contribution of winter mixing to eddy-Ekman pumping in the LCEs core primary production increase in winter. This issue was tackled by He et al. (2017) and Travis et al. (2019) comparing the rate of change of the mixed layer depth with the vertical velocity induced by the eddy-Ekman pumping (equation 4 in He et al, 2017). In the GoM, even if the wind shows larger magnitudes in winter, it is also associated with a large variability. As a consequence, the variability of Ekman pumping is also found large and a robust seasonal seasonal cycle which would allow to isolate the Ekman pumping in winter cannot be clearly identified. However, in the LCEs core, we estimate the mixed layer to deepen at roughly $0.8 \text{ m} \cdot \text{day}^{-1}$, which is on average about one order of magnitude larger than the higher bound of the estimated pumping mechanism typically occurring in winter in response to stronger wind events. This supports winter mixing as the overwhelming process for the LCEs-induced primary production peak in winter.

V/ Summary and perspectives

The [CHL] variability induced by the mesoscale Loop Current Eddies in the Gulf of Mexico is studied by analyzing vortex composite fields generated from a coupled physical-biogeochemical model at $1/12^\circ$ horizontal resolution. LCEs are hotspots for mesoscale biogeochemical variability. Despite the $[\text{CHL}]_{\text{surf}}$ negative anomaly associated with their core ($r < 50 \text{ km}$), model results indicate that LCEs are associated with enhanced phytoplankton biomass content, particularly in winter. This enhancement results from the contribution of multiple mechanisms of physical-biogeochemical interactions and contrasts with the background oligotrophic surface waters of the GoM.

The main results of this study are:

- LCEs cores present a negative surface chlorophyll anomaly,

- Unlike $[\text{CHL}]_{\text{surf}}$, $[\text{CHL}]_{\text{tot}}$ is larger in the LCEs cores compared to the background GoM in winter.
- LCEs core trigger a large phytoplankton biomass increase in winter,
- The winter mixing is a key mesoscale mechanism that preferentially supplies nutrients to the euphotic layer within the LCEs core. Consequently, it drives an eddy-induced peak of new primary production,
- Ekman-eddy pumping is a significant mechanism for sustaining relatively high new primary production rates within LCE cores during summer.

The phytoplankton biomass increase in individual LCEs cores suggests that LCEs play an important role in sustaining the large-scale GoM productivity.

GOLFO12-PISCES provides numerical results which were largely confronted to observations. This extensive validation gives confidence about its ability to produce realistic seasonal and mesoscale variability of biogeochemical tracers at surface and sub-surface, in particular the one associated with LCEs. However, biases are inherent to model and these results exposed in this study would require confirmation by sub-surface in-situ measurements within the core of LCEs.

Although the biological response to LCEs may present some specificities due to the particular dynamical nature of LCEs, this study suggests potentially generic insights on the biogeochemical role that anticyclonic eddies could play in oligotrophic environments. It echoes the previous works of Martin and Richards (2001), Gaube et al. (2014, 2015) and especially Dufois et al. (2014, 2016) and He et al. (2017) who proposed winter vertical mixing as an explanation for the positive $[\text{CHL}]_{\text{surf}}$ anomaly observed in anticyclones in the South Indian Ocean. One of the most crucial points to be underlined from our results is that the enhanced primary production and biomass content within anticyclonic eddies may not necessarily be correlated with the surface layer variability. In oligotrophic areas, the

549 integrated content of chlorophyll in the water column has to be considered. This implies that caution
550 should be exercised in the analysis and interpretation of $[\text{CHL}]_{\text{surf}}$ observed by remote sensing
551 instruments and highlights the crucial need for in-situ biogeochemical and bio-optical measurements.
552 In oligotrophic environments, defined by their low production rates and their low chlorophyll
553 concentration, anticyclonic eddies are able to trigger local enhanced biological productivity and
554 generate phytoplankton biomass positive anomalies. In a scenario of expansion of oligotrophic areas
555 (Barnett et al., 2001; Behrenfeld et al., 2006; Polovina et al., 2008), the fate and role of mesoscale
556 anticyclones is an important aspect to be considered.

557 This study focuses on mesoscale physical-biogeochemical interactions which is the spectral
558 range resolved by GOLFO12-PISCES configuration. It evidences the important role of mixing on
559 primary production in the LCE core at seasonal scale. However, mixing also presents significant
560 fluctuations at higher frequencies, associated with particular atmospheric events like storms. The PP_{tot}
561 response to such forcing requires further investigation to verify if the correlation between PP_{tot} and
562 mixing still hold on at higher frequencies where additional other drivers might also become important.
563 For instance, the role of submesoscale is of particular interest since it has been proved to trigger
564 mechanisms of significance importance for biogeochemistry (Levy et al., 2018). Higher model
565 resolutions can locally enhanced density gradients (Levy et al., 2012; Omand et al., 2015) leading to
566 ageostrophic circulations that perturbs the circular flow around vortices (Martin and Richards, 2001) or
567 enhanced vertical velocities that potentially foster the nutrient supply to the euphotic layer. Beside the
568 mesoscale Ekman pumping located at the eddy center, eddy-wind interactions also produce vertical
569 velocities at the eddy periphery (e.g. Flierl and McGillicuddy, 2002). Finally, it is also worth noting
570 that anticyclonic mesoscales eddies are capable of trapping near-inertial energy waves in the ocean
571 (Kunze 1985, Danioux et al. 2008, Koszalka et al. 2010, Pallas-Sanz et al., 2016) where they produce
572 vertical recirculation patterns (Zhong and Bracco, 2013). Even if, some of these dynamical aspects are

573 partially resolved at $1/12^\circ$ horizontal resolution, higher resolutions simulations with higher frequency
574 outputs are necessary to correctly assess their specific impact.

575 **Acknowledgments:** Research funded by the National Council of Science and Technology of Mexico –
576 Mexican Ministry of Energy – Hydrocarbon Trust, project 201441. This is a contribution of the Gulf of
577 Mexico Research Consortium (CIGoM). We acknowledge the provision of supercomputing facilities
578 by CICESE.

579 **APPENDIX A: CHL/C-biomass ratio and ecosystem structure**

580 [CHL] is widely used as a proxy for photosynthetic biomass (Strickland, 1965; Cullen, 1982).
581 However, in addition to depend on phytoplankton concentration, it is also affected by several other
582 factors mainly produced by intracellular physiological mechanisms (Geider, 1987). In particular,
583 photoacclimation processes have been proved to be determinant to explain [CHL]_{surf} variability in
584 oligotrophic areas (Mignot et al. 2014). In the GoM open-waters, this issue was specifically addressed
585 at a basin scale in Pasqueron de Fommervault et al. (2017) considering in-situ particulate
586 backscattering measurements and in Damien et al. (2018) from modeling tools. They both reach the
587 same conclusion: [CHL]_{tot} variability provides a reasonably good estimate of the total C-biomass
588 variability ([PHY]_{tot}).

589 This is confirmed by the small amplitude of the seasonal cycle of the ratio [CHL]_{tot}/[PHY]_{tot} in
590 the background GoM (0.256 +/- 0.004 g·mol⁻¹ averaged throughout the year, Fig A1). In the LCEs
591 core, this statement is still valid but must be qualified, since the ratio [CHL]_{tot}/[PHY]_{tot} presents small
592 but significant changes through the year (Fig A1.a). It is around 0.24 g·mol⁻¹ from March to November
593 and increases sharply in December to reach about 0.32 g·mol⁻¹ in January and February. As a result, in
594 winter, the photoacclimation mechanism accounts for ~25% of the total [CHL]_{tot} increase (the
595 remaining part being an effective phytoplankton biomass increase). In summer, the ratio
596 [CHL]_{tot}/[PHY]_{tot} is slightly lower in the LCEs core compared to the background GoM. As a
597 consequence, the [CHL]_{tot} negative anomaly associated with LCEs core does not necessarily translate
598 into a [PHY]_{tot} negative anomaly.

599 Overall in the GoM open-waters, there is a dominance of the small-size phytoplankton over the
600 large-size class in proportion closed to 80%-20% (Linacre et al., 2015). Although the modeled

ecosystem structure is relatively simple, this typical community size structure is well reproduced by GOLFO12-PISCES (Fig A1.c and A1.d), that also suggests a shift in the ecosystem structure in winter. The different response among size classes results from the enhancement of nutrient vertical flux. The role of “secondary” nutrient in this change in the community composition must not be overlooked also, in particular for diatoms (accounted in the model’s large-size group) since they also uptake on silicate (Benitez-Nelson et al., 2007). Moreover, GOLFO12-PISCES exhibits a modulation of the ecosystem structure by LCEs. The dominance of small-size phytoplankton is slightly more marked in summer and the winter shift is stronger in the LCEs core.

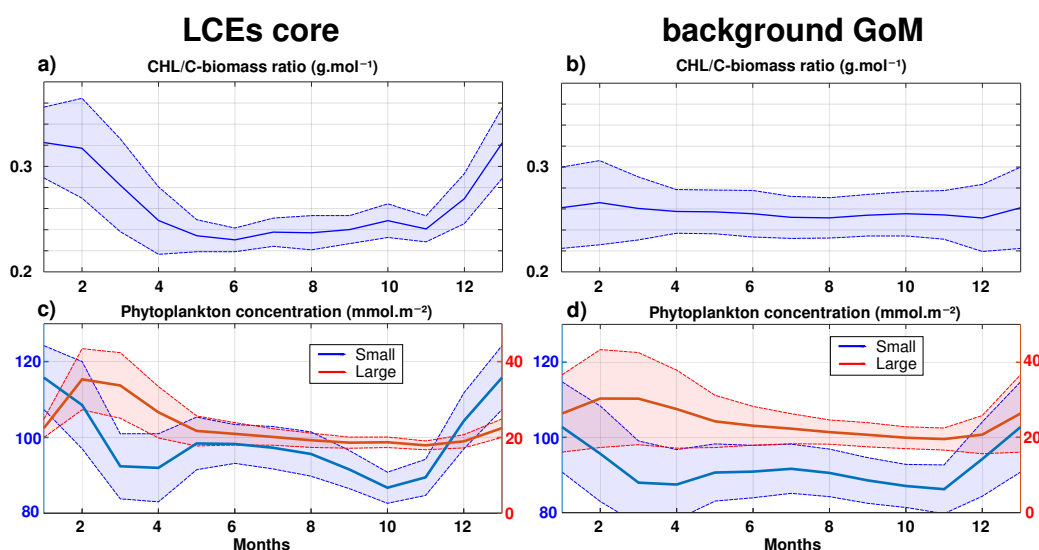


Figure A1: Climatological seasonal cycles of (a and b) the CHL/C-biomass ratio and (c and d) the vertically integrated content of phytoplankton concentration (small size in blue, large size in red). The left panels (a and c) refer to the time series in the LCEs core ($r < 50$ km) whereas the right panels (b and d) refer to the time series in the background GoM ($r > 200$ km). For each average cycle, the average value is shown (full line) along with its variability (± 1 standard deviation relative to the mean, dashed lines).

614 **APPENDIX B : Nitrate budget at a seasonal scale**

615 Nutrients availability in the euphotic layer is a key mechanism to trigger biomass increase in
 616 LCEs. The processes driving the seasonality of nutrient concentrations are here investigated diagnosing
 617 the different contributions to nitrate concentrations (hereafter [NO₃]) variability. The goal is to confirm
 618 the vertical transport of nutrients and quantify the budget in order to determine the driving mechanisms.
 619 The analysis is restricted to nitrate concentrations, considered as the main limiting factor for large size-
 620 class phytoplankton growth in the GoM (Myers et al., 1981; Turner et al., 2006), although phosphates
 621 and silicates are also modeled. We do not exclude that phosphates or silicates could also play a
 622 significant role. In cylindrical coordinates, the [NO₃] equation reads:

$$\begin{aligned}
 \frac{\partial NO_3}{\partial t} = & \underbrace{-V_r \frac{\partial NO_3}{\partial r}}_{\text{radial advection}} - \underbrace{\frac{V_\theta}{r} \frac{\partial NO_3}{\partial \theta}}_{\text{azimuthal advection}} - \underbrace{V_z \frac{\partial NO_3}{\partial z}}_{\text{vertical advection}} + \underbrace{\frac{D_l}{r} \frac{\partial}{\partial r} \left(r \frac{\partial NO_3}{\partial r} \right)}_{\text{lateral diffusion}} + \underbrace{\frac{D_l}{r^2} \frac{\partial^2 NO_3}{\partial \theta^2}}_{\text{lateral diffusion}} \\
 & + \underbrace{\frac{\partial}{\partial z} \left(K_z \frac{\partial NO_3}{\partial z} \right)}_{\text{vertical diffusion}} + \underbrace{SMS}_{\text{Source minus sink}} + Asselin
 \end{aligned}$$

624 Basically, this is a 3D advection-diffusion equation with added "sources and sinks" terms, namely
 625 biogeochemical release and uptake rates. One must include also an "Asselin term", a modeling artifact
 626 due to the Asselin time filtering. We focus on the seasonal cycle of three particular trend terms: the
 627 vertical mixing (Fig B1.a and B1.b), the vertical advection (Fig B1.c and B1.d) and a "source minus
 628 sink" term (Fig B1.e B1.f).

629 [NO₃] variations from vertical dynamics are mainly positive, especially in the first 100 m of the
 630 water column. This traduces in year-round NO₃ source driven by physical processes. By contrast,
 631 biogeochemical processes consume NO₃ in the upper layer to sustain the primary production (Fig B1.e
 632 and B1.f). In the sub-surface layer (~ below the isoline on which nitrate concentration is equal to 2
 633 mmol.m⁻³), the process of nitrification constitutes a biological source of [NO₃]. To first order, this

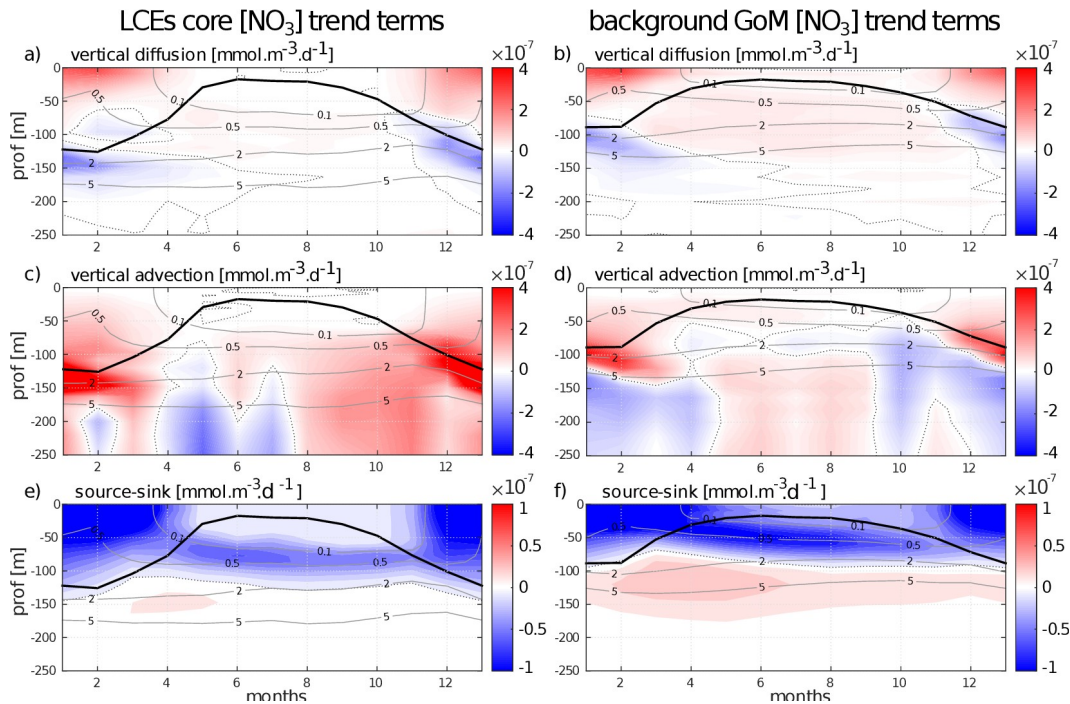
634 represents the global functioning of the ecosystem, valid in both fields and throughout the year.
635 However, the seasonal cycle strongly influence the magnitude of these trend terms, in particular in the
636 LCE core.

637 In winter, from December to February, vertical advective and diffusive motions produce an
638 increase of $[\text{NO}_3]$ within the mixed layer. This tendency consists in an advective entrainment resulting
639 from the deepening of the mixed layer which mainly acts to increase $[\text{NO}_3]$ at the base of the mixed
640 layer (Fig B1.c and B1.d) and vertical mixing which redistributes vertically the nutrients and tends to
641 homogenize $[\text{NO}_3]$ in the mixed layer (Fig B1.a and B1.b). The winter $[\text{NO}_3]$ increase is most important
642 in the LCE core at the base of the mixed layer ($\sim + 6.5 \cdot 10^{-7} \text{ mmol} \cdot \text{m}^{-3} \cdot \text{d}^{-1}$, nearly 3 times larger than in
643 the background GoM), attesting here a preferential NO_3 uplift due to deeper convection. Integrated
644 over the mixed layer, the winter vertical fluxes produce $[\text{NO}_3]$ enhancement of $\sim 2.4 \cdot 10^{-5} \text{ mmol} \cdot \text{m}^{-2} \cdot \text{d}^{-1}$
645 in the eddy core whereas it is only of $\sim 1.6 \cdot 10^{-5} \text{ mmol} \cdot \text{m}^{-2} \cdot \text{d}^{-1}$ in the background GoM. This also
646 explains why, on average, the density/nitrate relation differs in the LCEs core (Fig 5.e). In response, the
647 $[\text{NO}_3]$ tendency due to biogeochemical processes indicates an increase of the $[\text{NO}_3]$ uptake. This
648 increase is about 1.5 times larger in the core ($\sim - 1.3 \cdot 10^{-3} \text{ mmol} \cdot \text{m}^{-2} \cdot \text{d}^{-1}$ integrated over the mixed layer)
649 than in the background GoM ($\sim - 0.9 \cdot 10^{-3} \text{ mmol} \cdot \text{m}^{-2} \cdot \text{d}^{-1}$). Knowing that it feeds biomass production, this
650 $[\text{NO}_3]$ loss is consistent with the primary production peak in winter (Fig 9.e and 9.f).

651
652 In summer, $[\text{NO}_3]$ variations due to vertical processes are smaller than in winter. They are also
653 weaker in the LCEs core upper layer (almost nil in the 0-50m layer) compared to the background GoM,
654 consistent with a deeper NO_3 pool and a shallow mixer layer. In the eddy core, one can assume that the
655 NO_3 vertical supply is entirely consumed before reaching 50m. Below 50m, vertical $[\text{NO}_3]$ diffusive
656 trends are consistently more important in the background GoM, in agreement with a steeper nitracline
657 (Fig 5.e). In contrast, vertical $[\text{NO}_3]$ advective trends in the eddy core are similar to or can eventually

658 exceed the trends in the background GoM (as in September and October for example). This confirms a
 659 pumping mechanism to sustain primary production in summer within the eddy core (section V.4) The
 660 biogeochemical activity related to $[\text{NO}_3]$ variations is also less intense in summer compared to winter.
 661 The depth of maximum $[\text{NO}_3]$ uptake is located just above the DCM and $[\text{NO}_3]$ release below. The loss
 662 of $[\text{NO}_3]$ is about twice larger in the background GoM ($\sim -0.9 \cdot 10^{-7} \text{ mmol} \cdot \text{m}^{-3} \cdot \text{d}^{-1}$) than in the LCEs core
 663 ($\sim -0.5 \cdot 10^{-7} \text{ mmol} \cdot \text{m}^{-3} \cdot \text{d}^{-1}$). It is noteworthy that the biogeochemical $[\text{NO}_3]$ source term, namely the
 664 nitrification rate, is really low within the eddy core.

665 To close this analysis of the $[\text{NO}_3]$ budget, it must be said that lateral diffusion and Asselin
 666 tendencies are marginal terms compared to the others. Horizontal advection is of the same order of
 667 magnitude as the vertical terms and mainly acts to redistribute horizontally the NO_3 vertically moved
 668 (see supplementary material 1).



669 **Figure B1: Seasonal cycle of nitrate trend terms in the (left column) LCEs core and in the (right column) background GoM. The**
 670 **trend induced by (a and b) vertical mixing, the (c and d) vertical advection and the (e and f) biogeochemical source minus sink are**
 671 **represented. Isopycnals anomalies (gray contours) and the depth of the mixed layer (black line) are superimposed.**

672 **REFERENCES:**

- 673 Ascani, F., Richards, K. J., Firing, E., Grant, S., Johnson, K. S., Jia, Y., et al. (2013). Physical and
674 biological controls of nitrate concentrations in the upper subtropical North Pacific Ocean. *Deep Sea*
675 *Research, Part II*, 93, 119–134.
- 676 Aumont, O., & Bopp, L. (2006). Globalizing results from ocean in situ iron fertilization studies. *Global*
677 *Biogeochemical Cycles*, 20, GB2017. <https://doi.org/10.1029/2005GB002591>.
- 678 Aumont, O., Ethé, C., Tagliabue, A., Bopp, L., & Gehlen, M. (2015). PISCES-v2: An ocean
679 biogeochemical model for carbon and ecosystem studies. *Geoscientific Model Development*, 8(8),
680 2465–2513.
- 681 Badan Jr, A., Candela, J., Sheinbaum, J., & Ochoa, J. (2005). Upper-layer circulation in the approaches
682 to Yucatan Channel. *Washington DC American Geophysical Union Geophysical Monograph*
683 *Series*, 161, 57-69.
- 684 Barnett, T. P., Pierce, D. W., & Schnur, R. (2001). Detection of anthropogenic climate change in the
685 world's oceans. *Science*, 292(5515), 270-274.
- 686 Behrenfeld, M. J., O'Malley, R. T., Siegel, D. A., McClain, C. R., Sarmiento, J. L., Feldman, G. C., ...
687 & Boss, E. S. (2006). Climate-driven trends in contemporary ocean productivity. *Nature*, 444(7120),
688 752.

689 Benitez-Nelson, C. R., Bidigare, R. R., Dickey, T. D., Landry, M. R., Leonard, C. L., Brown, S. L., ...
690 & Bibby, T. S. (2007). Mesoscale eddies drive increased silica export in the subtropical Pacific Ocean.
691 *Science*, 316(5827), 1017-1021.

692 Biggs, D. C., & Ressler, P. H. (2001). Distribution and abundance of phytoplankton, zooplankton,
693 ichthyoplankton, and micronekton in the deepwater Gulf of Mexico. *Gulf of Mexico Science*, 19(1), 2.

694 Bracco, A., Provenzale, A., & Scheuring, I. (2000). Mesoscale vortices and the paradox of the
695 plankton. *Proceedings of the Royal Society of London B: Biological Sciences*, 267(1454), 1795-1800.

696 Brodeau, L., Barnier, B., Treguier, A.-M., Penduff, T., & Gulev, S. (2010). An ERA40-based
697 atmospheric forcing for global ocean circulation models. *Ocean Modelling*, 31, 88–104. [https://doi.org/](https://doi.org/10.1016/j.ocemod.2009.10.005)
698 [10.1016/j.ocemod.2009.10.005](https://doi.org/10.1016/j.ocemod.2009.10.005)

699 Brokaw, R. J., Subrahmanyam, B., & Morey, S. L. (2019), Loop current and eddy driven salinity
700 variability in the Gulf of Mexico, *Geophysical Research Letters*, 46, 5978–5986,
701 <https://doi.org/10.1029/2019GL082931>.

702 Chelton, D., DeSzoek, R., Schlax, M., El Naggar, K., & Siwertz, N. (1998). Geographical variability
703 of the first baroclinic Rossby radius of deformation. *Journal of Physical Oceanography*, 28(3), 433–
704 460.

705 Ciani, D., Carton, X., Aguiar, A. B., Peliz, A., Bashmachnikov, I., Ienna, F., ... & Santoleri, R. (2017).
706 Surface signature of Mediterranean water eddies in a long-term high-resolution simulation. *Deep Sea*
707 *Research Part I: Oceanographic Research Papers*, 130, 12-29.

708 Cooper, C., Forristall, G. Z., & Joyce, T. M. (1990). Velocity and hydrographic structure of two Gulf of
709 Mexico warm-core rings. *Journal of Geophysical Research: Oceans*, 95(C2), 1663-1679.

710 Cullen, J. J. (1982). The deep chlorophyll maximum: Comparing vertical profiles of chlorophyll a.
711 *Canadian Journal of Fisheries and Aquatic Sciences*, 39(5), 791–803.

712 Dai, A., & Trenberth, K. E. (2002). Estimates of freshwater discharge from continents: Latitudinal and
713 seasonal variations. *Journal of Hydro-meteorology*, 3, 660–687.

714 Damien, P., Pasqueron de Fommervault, O., Sheinbaum, J., Jouanno, J., Camacho-Ibar, V. F., &
715 Duteil, O. (2018). Partitioning of the Open Waters of the Gulf of Mexico Based on the Seasonal and
716 Interannual Variability of Chlorophyll Concentration. *Journal of Geophysical Research: Oceans*.

717 Danioux, E., Klein, P., & Rivière, P. (2008). Propagation of wind energy into the deep ocean through a
718 fully turbulent mesoscale eddy field. *Journal of Physical Oceanography*, 38(10), 2224-2241.

719 Dewar, W., and G. Flierl (1987), Some effects of the wind on rings, *J. Phys. Oceanogr.*, 17(10), 1653–
720 1667.

721 Doney, S. C., Glover, D. M., McCue, S. J., & Fuentes, M. (2003). Mesoscale variability of Sea-viewing
722 Wide Field-of-view Sensor (SeaWiFS) satellite ocean color: Global patterns and spatial scales. *Journal*
723 *of Geophysical Research: Oceans*, 108(C2).

724 Dong, C., X. Lin, Y. Liu, F. Nencioli, Y. Chao, Y. Guan, D. Chen, T. Dickey, and J. C. McWilliams
 725 (2012), Three-dimensional oceanic eddy analysis in the Southern California Bight from a numerical
 726 product, *J. Geophys. Res.*, 117, C00H14, doi:10.1029/2011JC007354.

727 Donohue, Kathleen A., et al. "Loop current eddy formation and baroclinic instability." *Dynamics of*
 728 *Atmospheres and Oceans* 76 (2016): 195-216.

729 d'Ovidio, F., De Monte, S., Della Penna, A., Cotté, C., & Guinet, C. (2013). Ecological implications of
 730 eddy retention in the open ocean: a Lagrangian approach. *Journal of Physics A: Mathematical and*
 731 *Theoretical*, 46(25), 254023.

732 Dufois, F., Hardman-Mountford, N. J., Greenwood, J., Richardson, A. J., Feng, M., Herbette, S., &
 733 Matear, R. (2014). Impact of eddies on surface chlorophyll in the South Indian Ocean. *Journal of*
 734 *Geophysical Research: Oceans*, 119(11), 8061-8077.

735 Dufois, F., Hardman-Mountford, N. J., Greenwood, J., Richardson, A. J., Feng, M., & Matear, R. J.
 736 (2016). Anticyclonic eddies are more productive than cyclonic eddies in subtropical gyres because of
 737 winter mixing. *Science advances*, 2(5), e1600282.

738 Dufois, F., Hardman-Mountford, N. J., Fernandes, M., Wojtasiewicz, B., Shenoy, D., Slawinski, D., ...
 739 & Toresen, R. (2017). Observational insights into chlorophyll distributions of subtropical South Indian
 740 Ocean eddies. *Geophysical Research Letters*, 44(7), 3255-3264.

741 Dugdale, R. C., and J. J. Goering (1967), Uptake of new and regenerated forms of nitrogen in primary
 742 productivity, *Limnol. Oceanogr.*, 12, 196–206

743 Early, J. J., Samelson, R. M., & Chelton, D. B. (2011). The evolution and propagation of
744 quasigeostrophic ocean eddies. *Journal of Physical Oceanography*, 41(8), 1535-1555.

745 Elliott, B. A. (1982). Anticyclonic rings in the Gulf of Mexico. *Journal of Physical Oceanography*,
746 12(11), 1292-1309.

747 Eppley, R. W., and B. J. Peterson (1979), Particulate organic matter flux and planktonic new
748 production in the deep ocean, *Nature*, 282, 677–680.

749 Falkowski, P., D. Ziemann, Z. Kolber, and P. Bienfang (1991), Role of eddy pumping in enhancing
750 primary production in the ocean, *Nature*, 352(6330), 55–58.

751 Flierl, G. R. (1981). Particle motions in large-amplitude wave fields. *Geophysical & Astrophysical*
752 *Fluid Dynamics*, 18(1-2), 39-74.

753 Flierl, G. R., & McGillicuddy, D. J. (2002). Mesoscale and submesoscale physical-biological
754 interactions. *The sea*, 12, 113-185.

755 de Fommervault, O. P., Perez-Brunius, P., Damien, P., Camacho-Ibar, V. F., & Sheinbaum, J. (2017).
756 Temporal variability of chlorophyll distribution in the Gulf of Mexico: bio-optical data from profiling
757 floats. *Biogeosciences*, 14(24), 5647.

758 Forristall, G. Z., Schaudt, K. J., & Cooper, C. K. (1992). Evolution and kinematics of a Loop Current
759 eddy in the Gulf of Mexico during 1985. *Journal of Geophysical Research: Oceans*, 97(C2), 2173-
760 2184.

761 Frolov, S. A., et al. "Loop Current eddy interaction with the western boundary in the Gulf of Mexico."
762 *Journal of physical oceanography* 34.10 (2004): 2223-2237.

763 Garcia-Jove Navarro, M., Sheinbaum Pardo, J., & Jouanno, J. (2016). Sensitivity of Loop Current
764 metrics and eddy detachments to different model configurations: The impact of topography and
765 Caribbean perturbations. *Atmosfera*, 29(3), 235–265. <https://doi.org/10.20937/ATM.2016.29.03.05>

766 Garçon, V. C., Oschlies, A., Doney, S. C., McGillicuddy, D., & Waniek, J. (2001). The role of
767 mesoscale variability on plankton dynamics in the North Atlantic. *Deep Sea Research Part II: Topical
768 Studies in Oceanography*, 48(10), 2199-2226.

769 Gaube, P., Chelton, D. B., Strutton, P. G., & Behrenfeld, M. J. (2013). Satellite observations of
770 chlorophyll, phytoplankton biomass, and Ekman pumping in nonlinear mesoscale eddies. *Journal of
771 Geophysical Research: Oceans*, 118(12), 6349-6370.

772 Gaube, P., McGillicuddy, D. J., Chelton, D. B., Behrenfeld, M. J., & Strutton, P. G. (2014). Regional
773 variations in the influence of mesoscale eddies on near-surface chlorophyll. *Journal of Geophysical
774 Research: Oceans*, 119(12), 8195-8220.

775 Gaube, P., Chelton, D. B., Samelson, R. M., Schlax, M. G., & O'Neill, L. W. (2015). Satellite
776 observations of mesoscale eddy-induced Ekman pumping. *Journal of Physical Oceanography*, 45(1),
777 104-132.

778 Geider, R. J. (1987), Light and temperature dependence of the carbon to chlorophyll a ratio in
779 microalgae and cyanobacteria: implications for physiology and growth of phytoplankton, *New Phytol.*,
780 106, 1–34.

781 Geider, R. J., MacIntyre, H. L., & Kana, T. M. (1997). A dynamical model of phytoplankton growth
782 and acclimation: Response of the balanced growth rate to light, nutrient limitation and temperature.
783 *Marine Ecology Progress Series*, 148, 187–200.

784 Glenn, S. M., and C. C. Ebbesmeyer (1993), Drifting buoy observations of a loop current
785 anticyclonic eddy, *J. Geophys. Res.*, , 98, 20, doi:10.1029/93JC02078.

786 Green, R. E., Bower, A. S., & Lugo-Fernández, A. (2014). First autonomous bio-optical profiling float
787 in the Gulf of Mexico reveals dynamic biogeochemistry in deep waters. *PloS one*, 9(7), e101658.

788 Guo, M., P. Xiu, S. Li, F. Chai, H. Xue, K. Zhou, and M. Dai (2017), Seasonal variability and
789 mechanisms regulating chlorophyll distribution in mesoscale eddies in the South China Sea, *J.*
790 *Geophys. Res. Oceans*, 122, 5329–5347, doi:10.1002/2016JC012670.

791 Hamilton, P., Leben, R., Bower, A., Furey, H., & Pérez-Brunius, P. (2018). Hydrography of the Gulf of
792 Mexico Using Autonomous Floats. *Journal of Physical Oceanography*, 48(4), 773-794. DOI: 10.1175/
793 JPO-D-17-0205.1

794 Hamilton, P. (2007). Eddy statistics from Lagrangian drifters and hydrography for the northern Gulf of
 795 Mexico slope. *Journal of Geophysical Research*, 112, C09002. <https://doi.org/10.1029/2006JC003988>

796 He, Q., Zhan, H., Shuai, Y., Cai, S., Li, Q. P., Huang, G., & Li, J. (2017). Phytoplankton bloom
 797 triggered by an anticyclonic eddy: The combined effect of eddy Ekman pumping and winter mixing.
 798 *Journal of Geophysical Research: Oceans*, 122(6), 4886-4901.

799 Hernandez-Guerra, A., & Joyce, T. M. (2000). Water masses and circulation in the surface layers of the
 800 Caribbean at 66 W. *Geophysical Research Letters*, 27(21), 3497–3500.
 801 <https://doi.org/10.1029/1999GL011230>

802 Herrmann, M., Somot, S., Sevault, F., Estournel, C., & Deque, M. (2008). Modeling the deep
 803 convection in the northwestern Mediterranean Sea using an eddy-permitting and an eddy-resolving
 804 model: Case study of winter 1986–1987. *Journal of Geophysical Research*, 113, C04011.
 805 <https://doi.org/10.1029/2006JC003991>

806 Huang, J., & Xu, F. (2018). Observational evidence of subsurface chlorophyll response to mesoscale
 807 eddies in the North Pacific. *Geophysical Research Letters*, 45, 8462–8470.
 808 <https://doi.org/10.1029/2018GL078408>

809 Jolliff, J. K., Kindle, J. C., Penta, B., Helber, R., Lee, Z., Shulman, I., Arnone, R., and Rowley, C. D.,
 810 (2008). On the relationship between satellite-estimated bio-optical and thermal properties in the Gulf of
 811 Mexico, *J. Geophys. Res.*, 113, G1, <https://doi.org/10.1029/2006JG000373>

812 Jouanno, J., Ochoa de la Torre, J. L., Pallas Sanz, E., Sheinbaum Pardo, J., Andrade Canto, F., Candela
 813 Perez, J., et al. (2016). Loop current frontal eddies: Formation along the Campeche Bank and impact of
 814 coastally trapped waves. *Journal of Physical Oceanography*, 46(11), 3339–3363.
 815 <https://doi.org/10.1175/JPO-D-16-0052.1>

816 Klein, P., & Lapeyre, G. (2009). The oceanic vertical pump induced by mesoscale and submesoscale
 817 turbulence. *Annual review of marine science*, 1, 351-375.

818 Koszalka, I. M., Ceballos, L., & Bracco, A. (2010). Vertical mixing and coherent anticyclones in the
 819 ocean: the role of stratification. *Nonlinear Processes in Geophysics*, 17(1), 37-47.

820 Kouketsu, S., Tomita, H., Oka, E., Hosoda, S., Kobayashi, T., & Sato, K. (2011). The role of meso-
 821 scale eddies in mixed layer deepening and mode water formation in the western North Pacific. In *New*
 822 *Developments in Mode-Water Research* (pp. 59-73). Springer, Tokyo.

823 Kunze, E. (1985). Near-inertial wave propagation in geostrophic shear. *Journal of Physical*
 824 *Oceanography*, 15(5), 544-565.

825 Lascaratos, A., & Nittis, K. (1998). A high-resolution three-dimensional numerical study of
 826 intermediate water formation in the Levantine Sea. *Journal of Geophysical Research*, 103(C9), 18497–
 827 18511.

828 Lehahn, Y., F. d'Ovidio, M. Levy, Y. Amitai, and E. Heifetz (2011), Long range transport of a quasi
 829 isolated chlorophyll patch by an Agulhas ring, *Geophys. Res. Lett.*, 38, L16610,
 830 [doi:10.1029/2011GL048588](https://doi.org/10.1029/2011GL048588).

831 Le Hénaff, M., Kourafalou, V. H., Morel, Y., & Srinivasan, A. (2012). Simulating the dynamics and
832 intensification of cyclonic Loop Current Frontal Eddies in the Gulf of Mexico. *Journal of Geophysical*
833 *Research: Oceans*, 117(C2).

834 Levitus, S. (1982). Climatological atlas of the world ocean (NOAA Prof. Pap. 13, 173 p.). Washington,
835 DC: U.S. Government Printing Office.

836 Lévy, M., Ferrari, R., Franks, P. J., Martin, A. P., & Rivière, P. (2012). Bringing physics to life at the
837 submesoscale. *Geophysical Research Letters*, 39(14).

838 Lévy, M., Franks, P.J.S. & Smith, K.S. (2018). The role of submesoscale currents in structuring marine
839 ecosystems. *Nat. Commun.*, **9**, 4758

840 Linacre, L., Lara-Lara, R., Camacho-Ibar, V., Herguera, J. C., Bazán-Guzmán, C., & Ferreira-Bartrina,
841 V. (2015). Distribution pattern of picoplankton carbon biomass linked to mesoscale dynamics in the
842 southern gulf of Mexico during winter conditions. *Deep Sea Research Part I: Oceanographic Research*
843 *Papers*, 106, 55-67.

844 Linacre, L., Durazo, R., Camacho-Ibar, V. F., Selph, K. E., Lara-Lara, J. R., Mirabal-Gómez, U., ... &
845 Sidón-Ceseña, K. (2019). Picoplankton Carbon Biomass Assessments and Distribution of
846 Prochlorococcus Ecotypes Linked to Loop Current Eddies During Summer in the Southern Gulf of
847 Mexico. *Journal of Geophysical Research: Oceans*, 124(11), 8342-8359.

848 Lipphardt, B., Poje, A. C., Kirwan, A., Kantha, L., & Zweng, M. (2008). Death of three Loop Current
849 rings. *Journal of Marine Research*, 66(1), 25-60.

850 Madec, G. (2016). NEMO ocean engine, Note Du Pole De Mod# elisation (Vol. 27, 406 p.). Paris,
851 France: Institut Pierre-Simon Laplace.

852 Mann, K. H., & Lazier, J. R. N. (2006). Dynamics of marine ecosystems (3rd ed.). Oxford, UK:
853 Blackwell Publishing.

854 Mahadevan, A. (2014). Ocean science: Eddy effects on biogeochemistry. *Nature*, 506(7487), 168.

855 Martin, A. P., & Richards, K. J. (2001). Mechanisms for vertical nutrient transport within a North
856 Atlantic mesoscale eddy. *Deep Sea Research Part II: Topical Studies in Oceanography*, 48(4-5), 757-
857 773.

858 Mayot, N., D'Ortenzio, F., Taillandier, V., Prieur, L., de Fommervault, O. P., Claustre, H., ... & Conan,
859 P. (2017). Physical and biogeochemical controls of the phytoplankton blooms in North Western
860 Mediterranean Sea: A multiplatform approach over a complete annual cycle (2012–2013 DEWEX
861 experiment). *Journal of Geophysical Research: Oceans*, 122(12), 9999-10019.

862 McClain, C. R., Signorini, S. R., & Christian, J. R. (2004). Subtropical gyre variability observed by
863 ocean-color satellites. *Deep Sea Research Part II: Topical Studies in Oceanography*, 51(1-3), 281-301.

864 McGillicuddy, D. J., Jr. (2016), Mechanisms of Physical-Biological-Biogeochemical Interaction at the
865 Oceanic Mesoscale, *Annu. Rev. Mar. Sci.*, 8, 125–159, doi:10.1146/annurev-marine-010814-015606.

866 McGillicuddy Jr, D. J., Robinson, A. R., Siegel, D. A., Jannasch, H. W., Johnson, R., Dickey, T. D., ...
867 & Knap, A. H. (1998). Influence of mesoscale eddies on new production in the Sargasso Sea. *Nature*,
868 394(6690), 263.

869 McGillicuddy Jr, D. J., & Robinson, A. R. (1997). Eddy-induced nutrient supply and new production in
870 the Sargasso Sea. *Deep Sea Research Part I: Oceanographic Research Papers*, 44(8), 1427-1450.

871 Meunier, T., Sheinbaum, J., Pallàs-Sanz, E., Tenreiro, M., Ochoa, J., Ruiz-Angulo, A., ... & de Marez,
872 C. (2020). Heat Content Anomaly and Decay of Warm-Core Rings: the Case of the Gulf of Mexico.
873 *Geophysical Research Letters*, 47(3), e2019GL085600.

874 Meunier, T., Tenreiro, M., Pallàs-Sanz, E., Ochoa, J., Ruiz-Angulo, A., Portela, E., et al. (2018a).
875 Intrathermocline eddies embedded within an anticyclonic vortex ring. *Geophysical Research Letters*,
876 45. <https://doi.org/10.1029/2018GL077527>

877 Meunier, T., Pallàs-Sanz, E., Tenreiro, M., Rodriguez, E. P., Ochoa, J., Ruiz-Angulo, A., & Cusí, S.
878 (2018b). The Vertical structure of a Loop Current Eddy. *Journal of Geophysical Research: Oceans*.

879 Mignot, A., Claustre, H., Uitz, J., Poteau, A., D'Ortenzio, F., and Xing, X., (2014), Understanding the
880 seasonal dynamics of phytoplankton biomass and the deep chlorophyll maximum in oligotrophic
881 environments: A Bio-Argo float investigation, *Global Biogeochem. Cy.*, 28, 856–876.

882 Monterey, G., & Levitus, S. (1997). Seasonal variability of mixed layer depth for the World Ocean
 883 (NOAA Atlas NESDIS 14, 100 p.). Silver Spring, MD: National Oceanic and Atmospheric
 884 Administration.

885 Muller-Karger, F. E., Walsh, J. J., Evans, R. H., & Meyers, M. B. (1991). On the seasonal
 886 phytoplankton concentration and sea surface temperature cycles of the Gulf of Mexico as determined
 887 by satellites. *Journal of Geophysical Research*, 96(C7), 12645–12665.

888 Myers, V. B., & Iverson, R. I. (1981). Phosphorus and nitrogen limited phytoplankton productivity in
 889 northeastern Gulf of Mexico coastal estuaries. In *Estuaries and nutrients* (pp. 569-582). Humana Press.

890 Nencioli, F., C. Dong, T. Dickey, L. Washburn, and J. C. McWilliams (2010), A vector geometry-
 891 based eddy detection algorithm and its application to a high-resolution numerical model product and
 892 high-frequency radar surface velocities in the Southern California Bight, *J. Atmos. Oceanic Technol.*,
 893 27, 564–579, doi:10.1175/2009JTECHO725.1.

894 Nof, D., 1981: On the b-induced movement of isolated baroclinic eddies. *J. Phys. Oceanogr.*, 11, 1662–
 895 1672, [https://doi.org/ 10.1175/1520-0485\(1981\)011,1662:OTIMOI.2.0.CO;2](https://doi.org/10.1175/1520-0485(1981)011<1662:OTIMOI.2.0.CO;2).

896 Nowlin, W. D. Jr., & Parker, C. A. (1974). Effects of a cold-air outbreak on shelf waters of the Gulf of
 897 Mexico. *Journal of Physical Oceanography*, 4(3), 467–486.

898 Omand, M. M., D’Asaro, E. A., Lee, C. M., Perry, M. J., Briggs, N., Cetinić, I., & Mahadevan, A.
 899 (2015). Eddy-driven subduction exports particulate organic carbon from the spring bloom. *Science*,
 900 348(6231), 222-225.

901 Omand, M. M., & Mahadevan, A. (2014). Shape of the oceanic nitracline. *Biogeosciences Discussions*,
902 11, 14729–14763.

903 Oschlies, A., & Garcon, V. (1998). Eddy-induced enhancement of primary production in a model of the
904 North Atlantic Ocean. *Nature*, 394(6690), 266.

905 Pallàs-Sanz, E., Candela, J., Sheinbaum, J., Ochoa, J., & Jouanno, J. (2016). Trapping of the near-
906 inertial wave wakes of two consecutive hurricanes in the Loop Current. *Journal of Geophysical*
907 *Research: Oceans*, 121(10), 7431-7454.

908 Passalacqua, G. A., Sheinbaum, J., & Martinez, J. A. (2016). Sea surface temperature influence on a
909 winter cold front position and propagation: Air-sea interactions of the ‘Nortes’ winds in the Gulf of
910 Mexico. *Atmospheric Science Letters*, 17(5), 302–307.

911 Polovina, J. J., Howell, E. A., & Abecassis, M. (2008). Ocean's least productive waters are expanding.
912 *Geophysical Research Letters*, 35(3).

913 Sathyendranath, S, Brewin, RJW, Müeller, D, Brockmann, C, Deschamps, P-Y, Doerffer, R, Fomferra,
914 N, Franz, BA, Grant, MG, Hu C, Krasemann, H, Lee, Z, Maritorena, S, Devred, E, Mélin, F, Peters, M,
915 Smyth, T, Steinmetz, F, Swinton, J, Werdell, J, Regner, P (2012) Ocean Colour Climate Change
916 Initiative: Approach and Initial Results, IGARSS 2012, 2024-2027.
917 doi:10.1109/IGARSS.2012.6350979.

918 Sheinbaum Pardo, J., Athie De Velasco, G. E., Candela Perez, J., Ochoa de la Torre, J. L., & Romero
 919 Arteaga, A. M. (2016). Structure and variability of the Yucatan and loop currents along the slope and
 920 shelf break of the Yucatan channel and Campeche bank. *Dynamics of Atmospheres and Oceans*, 76,
 921 217–239. <https://doi.org/10.1016/j.dynatmoce.2016.08.001>

922 Sherr, E. B., & Sherr, B. F. (2002). Significance of predation by protists in aquatic microbial food
 923 webs. *Antonie van Leeuwenhoek*, 81(1), 293-308.

924 Siegel, D. A., Behrenfeld, M. J., Maritorena, S., McClain, C. R., Antoine, D., Bailey, S. W., ... & Eplee
 925 Jr, R. E. (2013). Regional to global assessments of phytoplankton dynamics from the SeaWiFS
 926 mission. *Remote Sensing of Environment*, 135, 77-91.

927 Siegel, D. A., McGillicuddy Jr, D. J., & Fields, E. A. (1999). Mesoscale eddies, satellite altimetry, and
 928 new production in the Sargasso Sea. *Journal of Geophysical Research: Oceans*, 104(C6), 13359-
 929 13379.

930 Sosa-Gutiérrez, R., et al. "Erosion of the Subsurface Salinity Maximum of the Loop Current Eddies
 931 From Glider Observations and a Numerical Model." *Journal of Geophysical Research: Oceans* 125.7
 932 (2020): e2019JC015397.

933 Strickland, J. D. H. (1965). Production of organic matter in the primary stages of the marine food
 934 chain, *Chem. Oceanogr.*, 1, 477–610.

935 Sturges, W., & Leben, R. (2000). Frequency of ring separations from the Loop Current in the Gulf of
 936 Mexico: A revised estimate. *Journal of Physical Oceanography*, 30, 1814–1819.

- 937 Sturges, W., & Kenyon, K. E. (2008). Mean flow in the Gulf of Mexico. *Journal of Physical*
938 *Oceanography*, 38(7), 1501-1514.
- 939 Sweeney, E. N., D. J. McGillicuddy, and K. O. Buesseler (2003), Biogeochemical impacts due to
940 mesoscale eddy activity in the Sargasso Sea as measured at the Bermuda Atlantic Time-series Study
941 (BATS), *Deep Sea Res., Part II*, 50(22–26), 3017–3039, doi:10.1016/j.dsr2.2003.07.008.
- 942 Tenreiro, M., Candela, J., Sanz, E. P., Sheinbaum, J., & Ochoa, J. (2018). Near-Surface and Deep
943 Circulation Coupling in the Western Gulf of Mexico. *Journal of Physical Oceanography*, 48(1), 145-
944 161.
- 945 Travis, S., & Qiu, B. (2020). Seasonal Reversal of the Near-Surface Chlorophyll Response to the
946 Presence of Mesoscale Eddies in the South Pacific Subtropical Countercurrent. *Journal of Geophysical*
947 *Research: Oceans*, 125(3), e2019JC015752.
- 948 Turner, J. S. (1973). Buoyancy effects in fluids (368 p.). New York, NY: Cambridge University Press.
- 949 Turner, R. E., Rabalais, N. N., & Justic, D. (2006). Predicting summer hypoxia in the northern Gulf of
950 Mexico: Riverine N, P, and Si loading. *Marine pollution bulletin*, 52(2), 139-148.
- 951 Vukovich, F. M., 2007: Climatology of ocean features in the Gulf of Mexico using satellite remote
952 sensing data. *J. Phys. Oceanogr.*, 37, 689–707, <https://doi.org/10.1175/JPO2989.1>.

953 Waite, A. M., S. Pesant, D. A. Griffin, P. A. Thompson, and C. M. Holl (2007), *Oceanography*,
 954 primary production and dissolved inorganic nitrogen uptake in two Leeuwin Current eddies, *Deep Sea*
 955 *Res., Part II*, 54(8–10), 981–1002, doi:10.1016/j.dsr2.2007.03.001.

956 Wawrik, B., Paul, J., Bronk, D., John, D., Gray, M., 2004. High rates of ammonium recycling drive
 957 phytoplankton productivity in the offshore Mississippi River plume. *Aquat. Microb. Ecol.* 35, 175–184.
 958 <http://dx.doi.org/10.3354/ame035175>.

959 Weisberg, R. H., & Liu, Y. (2017). On the Loop Current penetration into the Gulf of Mexico. *Journal*
 960 *of Geophysical Research: Oceans*, 122(12), 9679–9694.

961 Williams, R. G. (1988). Modification of ocean eddies by air-sea interaction. *Journal of Geophysical*
 962 *Research: Oceans*, 93(C12), 15523–15533.

963 Wu, G. (1964). Stratification and circulation in the Antillean-Caribbean basins (Vol. 1). New York,
 964 NY: Columbia University Press.

965 Zhao, J., Bower, A., Yang, J., & Lin, X. (2018). Meridional heat transport variability induced by
 966 mesoscale processes in the subpolar North Atlantic. *Nature communications*, 9(1), 1124.

967 Zhong, Y., & Bracco, A. (2013). Submesoscale impacts on horizontal and vertical transport in the Gulf
 968 of Mexico, *Journal of Geophysical Research: Oceans*, 118(10), 5651–5668.